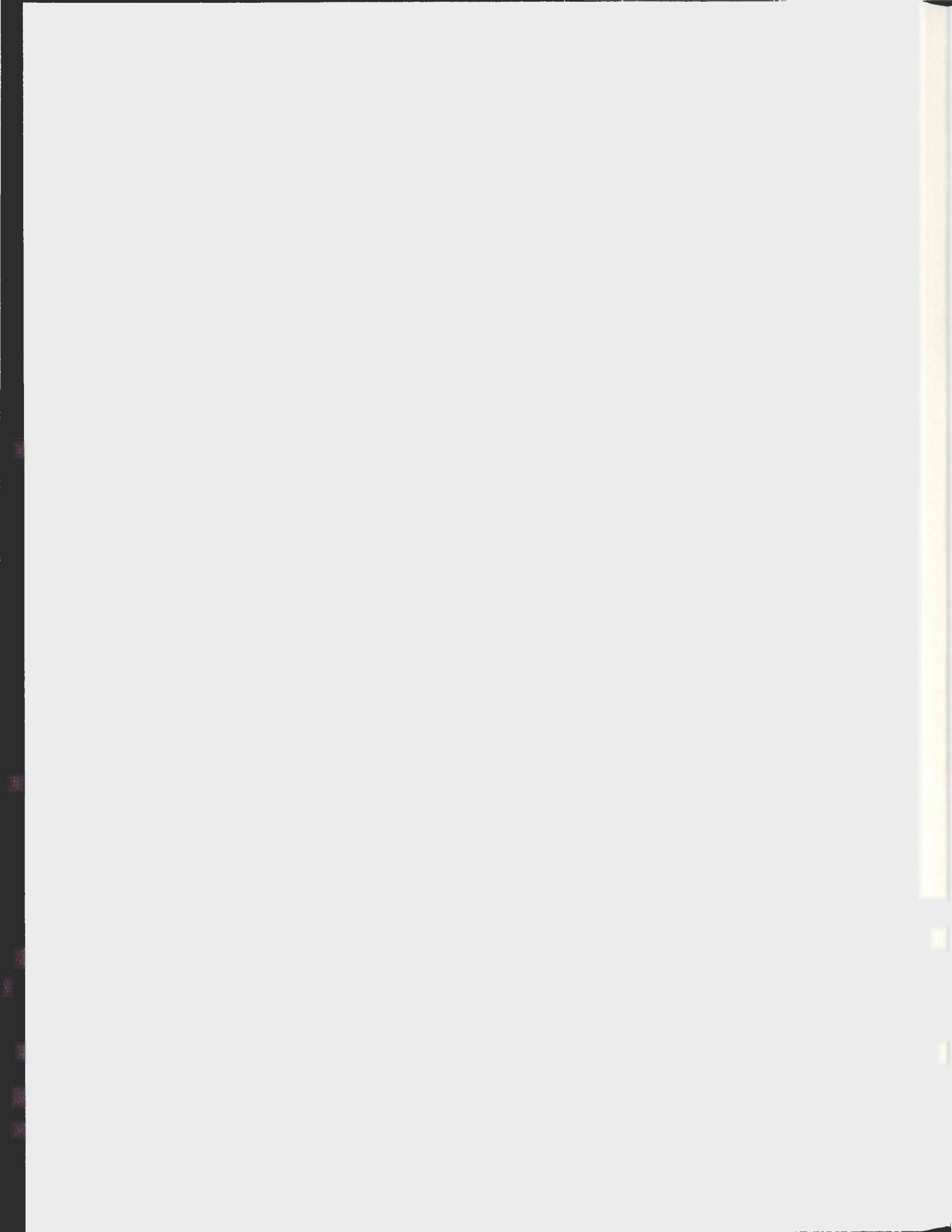


SILL PROCESSES IN THE SAGUENAY FJORD

DAVID C. JAMES



Sill Processes in the Saguenay Fjord

by

© David C. Janes
B.Sc (Applied Math and Physics)

A thesis submitted to the
School of Graduate Studies
in partial fulfillment of the
requirements for the degree of
Master of Science.

Environmental Science Program
Memorial University

February 9, 2008

ST. JOHN'S

NEWFOUNDLAND

Contents

Abstract	iv
Acknowledgements	v
List of Figures	x
1 Introduction	1
1.1 Fjords and sill processes	1
1.2 The Saguenay Fjord	5
1.3 Objectives	9
2 Simulations	10
2.1 Introduction	10
2.2 Methods	10
2.2.1 Model	10
2.2.2 Analysis	15
2.3 Results	18
2.3.1 Flow structure	18
2.3.2 Kinetic Energy	24
2.4 Discussion	28

3	Field Observations	30
3.1	Introduction	30
3.2	Methods	30
3.2.1	Sampling	30
3.2.2	Data Analysis	33
3.3	Results	34
3.3.1	A large-amplitude wavetrain	34
3.3.2	Evidence of internal wave reflection	45
3.4	Discussion	55
4	Summary	57
	Bibliography	59
A	Geo-rectification how-to	62
A.1	Introduction	62
A.2	On-Site Set-Up	62
A.3	Rectification	63
A.3.1	g_rect package	63
A.4	.dat file	64
A.5	Ground Control Points	65
A.6	g_rect.m	69
A.7	show_rectification.m	69
B	Validating temporal to spatial ADCP transformation	74
B.1	Phase speed of the wave	74
B.2	Validating	74

Abstract

Numerical simulations with a two-dimensional computer model are used in conjunction with a field study to examine sill processes near the shallow inner sill of the Saguenay Fjord, Quebec. The simulations predict that areas close to each side of the sill show enhanced turbulence, which could lead to the generation of internal waves and mixing. Spatial and temporal kinetic energies on each side of the sill are discussed along with their use to aid in planning a field study of the area. Field observations collected during Summer 2007 resulted in 23 internal wavetrains being sampled, propagating in nearly every direction on both sides of the sill. The cross-channel motion of some of these wavetrains could not be predicted by the model as it is two-dimensional. The use of a small, easily maneuverable boat for sampling resulted in the ability to sample a wavetrain more than once as it propagates. Shore-based photography from nearby hills were also collected providing a time-lapsed data set showing the sea surface manifestations. A large-amplitude internal wavetrain is discussed along with perhaps the first ever documented occurrence of internal wave reflection in a coastal environment.

Acknowledgements

I would like to thank my Masters supervisor Dr. Daniel Bourgault whose constant guidance and willingness to help proved invaluable throughout this project.

Special thanks also go out to Dr. Peter Galbraith and Rémi Desmarais for their assistance during the field study, and to Chris Stevenson in helping me with the seemingly endless number of computer related questions I had.

I would also like to thank all of my peers at the Physics and Physical Oceanography Department and the entire SLEIWEX team for their assistance during my Masters.

List of Figures

1.1	Results from the two-dimensional nonhydrostatic numerical simulations of Afanasyev and Peltier (2001) showing the progression of flow of an internal lee wave breaking on the Knight Inlet sill (timing - $a = 4$ minutes, $b = 8$ minutes, $c = 12$ minutes, $d = 14$ minutes). The arrows show the typical features of wave breaking.	3
1.2	Field observations of Klymak and Gregg (2003) showing flow structure (gray scale, backscatter) and dissipation rates of turbulent kinetic energy ϵ (color profiles 15769 to 15772) along the Knight Inlet sill at the end of ebb tide. These observations show evidence of the breaking of a large-amplitude lee wave.	4
1.3	Field observations of Farmer and Armi (1999) showing internal waves trapped above the sill crest in Knight Inlet. The upper panel shows data taken two hours before the lower panel.	6
1.4	Mercator projection of the Saguenay Fjord. The red T indicates the location of Tadoussac, a community at the mouth of the fjord. 1, 2, 3 show the locations of the outer sill, shallow inner sill, and deep inner sill, respectively, while 4 indicates the location of the bend in the fjord and also the cape Pointe aux Crêpes which is a location of internal wave reflection discussed in Chapter 3.	7

2.1	Schematic diagram of the model geometry (From Bourgault and Kelley, 2004)	12
2.2	Horizontal resolution. The grid size is $\Delta x_{\min} = 3.5$ m 2000 m on each side of the sill, increasing by a stretch factor of 1.1 to $\Delta x_{\max} = 1000$ m.	13
2.3	Vertical resolution. The grid size is $\Delta z_{\min} = 1$ m for the first 160 m of depth, increasing by a stretch factor of 1.1 to $\Delta z_{\max} = 10$ m.	14
2.4	Width $B(x, z)$ and depth $H(x)$ of the fjord interpolated on a variable grid with maximum horizontal resolution ($\Delta x_{\min} = 3.5$ m) centered around the inner sill (i.e. at $x = 0$).	14
2.5	The left panel shows the density profile used for the stratified case (solid) and the unstratified case (dotted). The right panel shows the corresponding buoyancy frequency for the stratified case.	16
2.6	Details of the depth and width around the inner sill where maximum resolution ($\Delta x = 3.5$ m) is used. The vertical black line delimits the two regions on each side of the sill where the temporal variations of the kinetic energy (see Equation 2.12) is calculated.	18
2.7	Images show the progression of tidal flow for the unstratified case using the passive tracer C . τ is the time in hours with respect to low water at Tadoussac with $\tau = 0$ being at the low water mark. The passive tracer is only used for visualization with the units being arbitrary.	19
2.8	Images show the progression of tidal flow for the stratified case using the passive tracer C	20
2.9	Images show the progression of tidal flow in the stratified case using u	22
2.10	Images show the progression of tidal flow in the stratified case using w	23
2.11	Internal wavetrain propagating seaward at $\tau = 8.43$ h. For plotting the vectors the mean horizontal current has been removed.	24

2.12	Example of Reynold's decomposition on a cell located at $x = -1251$ m, $z = 31$ m. The top panel is u , the middle panel is $\langle u \rangle$ and the bottom panel is u'	25
2.13	Fluctuation from mean kinetic energy for the stratified (bottom) and unstratified (top) cases. The color scales have been forced to be the same.	26
2.14	Timeseries of total fluctuation from the mean kinetic energy for the stratified (solid) and unstratified (dotted) simulations. Red corresponds to the landward side of the sill while black is for the seaward side.	27
2.15	Field observations from Klymak and Gregg (2003) showing the turbulent dissipation rate near the sill in Knight Inlet. Landward is positive on the x-axis.	29
3.1	Zoom of the shallow inner sill of the Saguenay Fjord. Location for the field study presented in this chapter.	31
3.2	GPS tracks for July 9th. The 'X' represents the location of the cameraman.	35
3.3	Backscatter intensity plots for the four passes made through an internal wave train on July 9th, 2007.	37
3.4	Density profiles of the water structure prior to wavetrains G (black) and H (red) passing through.	38
3.5	Intensity, horizontal velocities u and v , and vertical velocity w for track G on July 9, 2007. The white dotted line in the intensity plot shows the location of the VMP profile used to calculate σ_t displayed in Figure 3.4.	39

3.6	Intensity, horizontal velocities u and v , and vertical velocity w for track H on July 9, 2007.	40
3.7	Georectification image showing wavetrain G. The black line indicates the GPS track of the Krill, which is out of sight of the camera in this frame, but is still collecting data.	41
3.8	Same as Figure 3.7 for wavetrain H. The black line shows the GPS track, while the red 'X' indicates the location of the Krill.	42
3.9	Wavetrains G and H transformed to the spatial domain.	43
3.10	Location (X) and field of view of the camera (lines) for July 5(1) and 10(2), 2007. The blue lines on the coastline indicate where the waves reflect.	46
3.11	Density profile of the water column before wavetrain E propagates through.	47
3.12	Intensity, horizontal velocities u and v , and vertical velocity w initial incoming wave on July 5, 2007 which later is reflected off the coastline.	48
3.13	Internal wave bands spreading nearly across the entire width of the fjord prior to being 'cut' at Pointe aux Crêpes. The image was taken at 17:40 UTC. Refer to Figure 3.16 for a detailed temporal view around the cape.	49
3.14	GPS tracks for train E and train F which is sampled 10 minutes later. The red circle indicates an area where a second camera would be useful to document the flow up-fjord.	50
3.15	Intensity, horizontal velocities u and v , and vertical velocity w for wavetrain F.	51

3.16	Progression figure for wave reflection on July 5, 2007. The lines correspond to the wave crests while the arrows indicate the direction the waves are propagating. The red 'X' in the first four panels indicates the location of the Krill.	52
3.17	Progression figure for wave reflection on July 10, 2007.	54
A.1	Sample image of the Saguenay Fjord. (a) highlights a boat which has a GPS and the corresponding lat and lon can be obtained for the time this picture was taken. (b) highlights a small cape whose lat and lon can easily be obtained from a marine chart.	66
A.2	Zoom of the boat in order to obtain the x and y pixels.	67
A.3	Zoom of the cape in order to obtain x and y pixels.	68
A.4	Full rectified image. GCPs are show as red x's and ICPs are blue circles. The black x indicates the location of the camera.	72
A.5	Zoom of rectified image showing internal wavetrain.	73
B.1	Two georectified images spaced five minutes apart are used to calculate the phase speed of the internal wavetrain. The latitude and longitude of the black (red) dots on the left panel along with those from the right panel are used to find the distance traveled by the wavetrain in five minutes.	75
B.2	Three dots on one wave crest are matched with the corresponding ones on another crest to find the wavelength of the internal wavetrain. The result is the average of the values.	77
B.3	In two cases the peak to peak distance is used to find the wavelength, while in another the trough to trough distance is used. The average value is used to compare to that obtained from Figure B.2	78

Chapter 1

Introduction

1.1 Fjords and sill processes

A fjord is formed when an area carved out by glacial activity becomes filled with water (Trujillo and Thurman, 2005). Historically, the word fjord has been used to describe a variety of marine environments, from freshwater lakes to more intricate coastal systems. Today it is more commonly used for semi-enclosed coastal inlets, which may also be referred to as sounds, inlets or arms.

Fjords are long compared to their width, surrounded by steep cliffs, are deep relative to the adjacent continental shelf and often contain at least one submarine sill which separates the fjord into basins. As well, they most commonly occur at high latitudes and have a freshwater influx at the head (Farmer and Freeland, 1983).

When stratified flow encounters changes in the bottom bathymetry of a fjord, such as a sill, processes like internal waves and turbulence can occur. The study of stratified fluids over topography has garnered a lot of interest in the scientific community with its understanding having importance to both oceanography and atmospheric science (Baines, 1984).

One area that has received a lot of attention in this topic is Knight Inlet, on the coast of British Columbia. According to Lamb (2004), the sill in Knight Inlet is like a natural laboratory for studying stratified flow over an obstacle due to it being relatively straight and possessing a near two dimensional flow during ebb tide, making it easier to simulate with computer models.

Afanasyev and Peltier (2001) use numerical simulations to examine internal waves breaking on the sill in Knight Inlet. Figure 1.1 shows the progression of a wave breaking on the sill typical of those found in various model runs. They found the breaking of these waves resulted in irreversible mixing which extends downstream from the point of breaking.

Lamb (2004) used a non-hydrostatic two dimensional model to study stratified tidal flow over the Knight Inlet sill. He found that in 10 of his 11 model runs large lee waves were formed near the sill. The waves would grow, then break creating a high pressure region needed to create a high-drag state.

Knight Inlet has also been the site of many field studies concerned with stratified flow over topography. Klymak and Gregg (2003) used over 745 profiles near the sill to measure the dissipation of kinetic energy. One instrument used for these profiles was an Advanced Microstructure Profiler (AMP). The AMP is equipped with a suite of sensors to measure microscale (\sim mm-cm) flow characteristics such as shear and temperature gradients. From the microscale shear measurements, the dissipation rate of turbulent kinetic energy ϵ can be calculated (Osborn, 1974).

Figure 1.2 shows an illuminating example of their observations. The continuous record of echo-sounder observations combined with the AMP profiles of ϵ provides a clear picture of a breaking lee wave during ebb tide. Upstream (profiles 15769 - 15770), the turbulence was found to be low, while high dissipation rates were found throughout the water column in the undular wave (profile 15771).

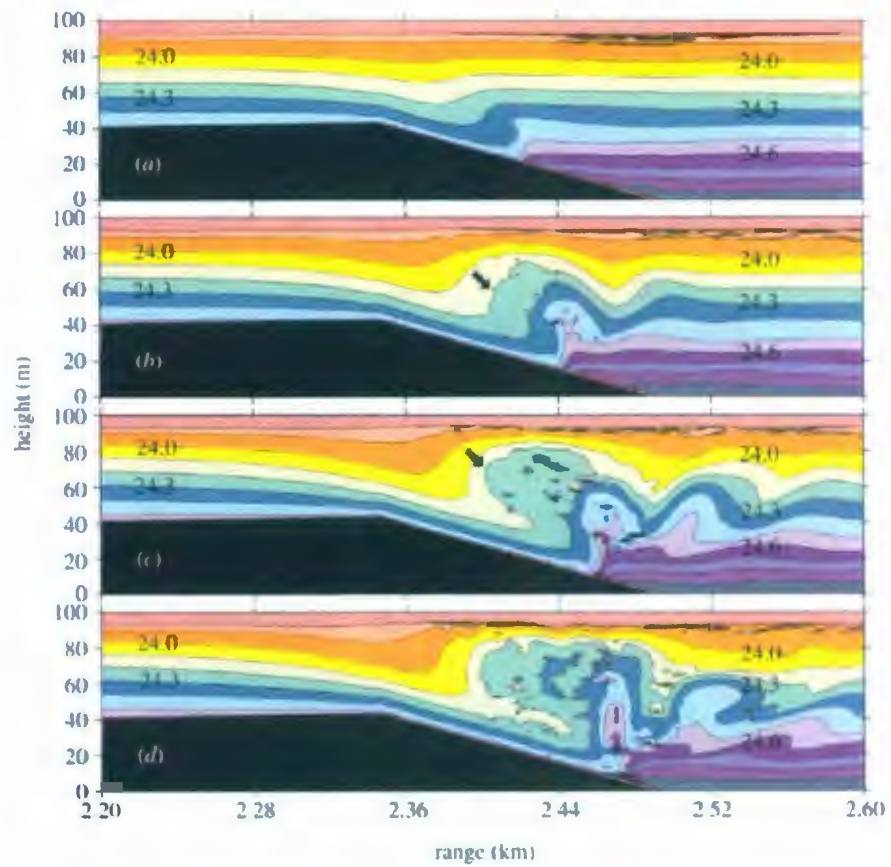


Figure 1.1: Results from the two-dimensional nonhydrostatic numerical simulations of Afanasyev and Peltier (2001) showing the progression of flow of an internal lee wave breaking on the Knight Inlet sill (timing - $a = 4$ minutes, $b = 8$ minutes, $c = 12$ minutes, $d = 14$ minutes). The arrows show the typical features of wave breaking.

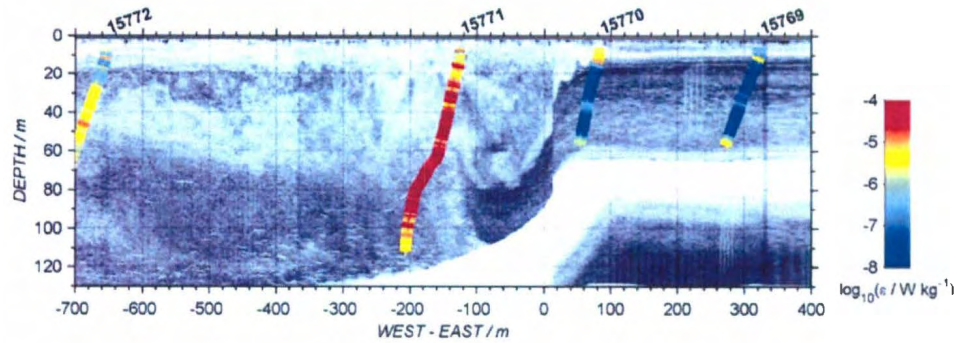


Figure 1.2: Field observations of Klymak and Gregg (2003) showing flow structure (gray scale, backscatter) and dissipation rates of turbulent kinetic energy ϵ (color profiles 15769 to 15772) along the Knight Inlet sill at the end of ebb tide. These observations show evidence of the breaking of a large-amplitude lee wave.

Similar processes occur during flood tide on the other side of the sill. Averaged over many tidal cycles, they observed high dissipation rates, of order $10^{-4} \text{ W kg}^{-1}$, on both sides of the Knight Inlet sill. They attributed these high level of turbulence to shear instabilities and breaking lee waves. Note also the qualitative but striking similarities between these field observations (Figure 1.2) and the numerical simulations of Afanasyev and Peltier (2001) presented in Figure 1.1.

Since the pioneering work of Farmer and Freeland (1983), several field studies have been conducted on the generation of internal waves near the Knight Inlet sill. Cummins *et al.* (2003) used echosounder and velocity measurements, along with photographic images of the surface signature to examine the generation and propagation of internal waves in Knight Inlet. They found waves being generated upstream of the sill and when the tidal flow relaxed the waves would propagate upstream. They coupled these observations with results from a numerical model which found that an undular bore was formed upstream of the sill due to rapidly increasing tidal forcing

and upstream influence. When the tidal flow relaxed the bore became a group of propagating internal waves, similar to those in the observations. They make the statement that this process of generation likely has application in other areas of stratified flow over topography.

Farmer and Armi (1999) observed internal wave being trapped over the sill in Knight Inlet (Figure 1.3). They found internal waves formed upstream of the sill crest were allowed to propagate away from the sill, while those downstream of the crest became trapped.

From Figure 1.3 we see an internal wave train which has been trapped for nearly two hours. Farmer and Armi indicate that trapped waves maintain their amplitude, leading them to believe that growth is balanced by dissipation of the wave. Once the tidal flow decreases these trapped waves are allowed to escape.

1.2 The Saguenay Fjord

All of the attributes mentioned before in defining fjords can be used to describe the Saguenay Fjord, which is the location of the study discussed in this thesis. The Saguenay Fjord (Figure 1.4) is located on the east coast of Quebec approximately 200 km northwest of Quebec City and is the most southernly northeast American Fjord (Stacey and Gratton, 2001).

Its overall length is approximately 120 km with its width ranging from 1-4 km and an average width of 2 km. Three sills exist in the Saguenay Fjord; the first is a shallow (30 m) sill near the mouth, the second occurs 20 km inland with a depth of 60 m and the third is 30 km inland with a depth of 120 m (see annotations on Figure 1.4). This thesis will adopt the naming convention of outer sill, shallow inner sill, and deep inner sill, respectively. These sills break the fjord into 3 basins varying

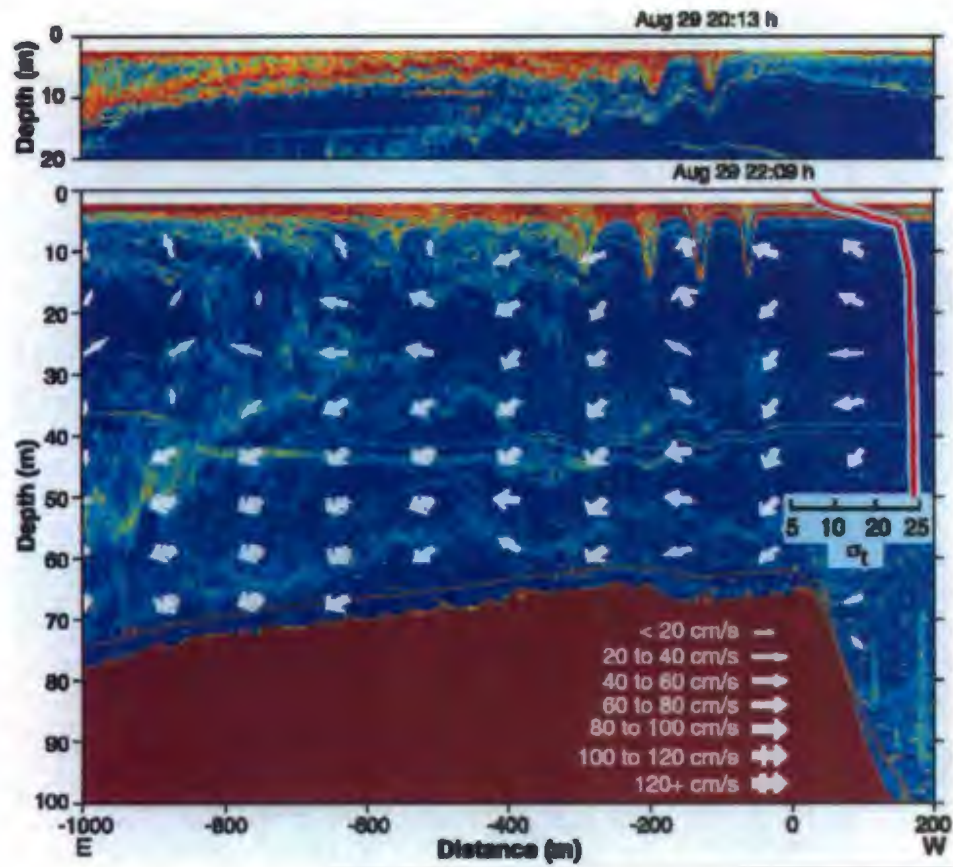


Figure 1.3: Field observations of Farmer and Armi (1999) showing internal waves trapped above the sill crest in Knight Inlet. The upper panel shows data taken two hours before the lower panel.

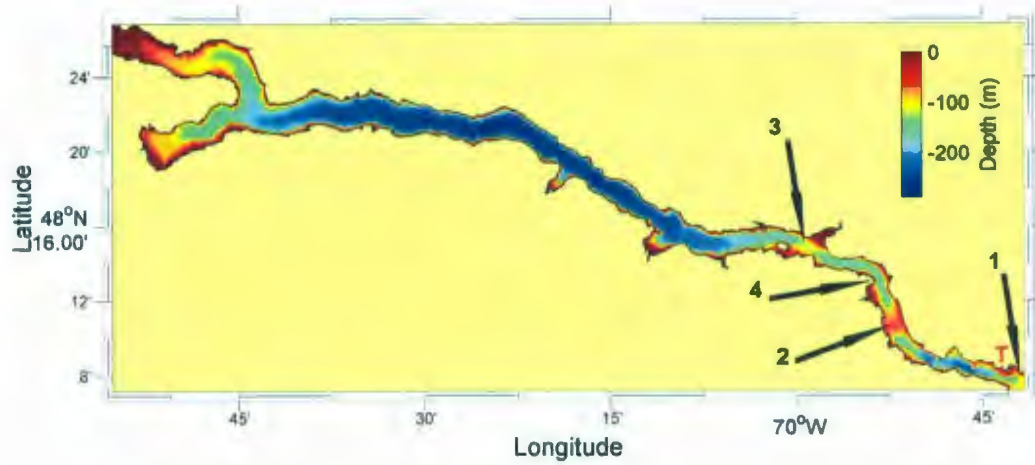


Figure 1.4: Mercator projection of the Saguenay Fjord. The red T indicates the location of Tadoussac, a community at the mouth of the fjord. 1, 2, 3 show the locations of the outer sill, shallow inner sill, and deep inner sill, respectively, while 4 indicates the location of the bend in the fjord and also the cape Pointe aux Crêpes which is a location of internal wave reflection discussed in Chapter 3.

in depth from 180 m to 280 m. The basin between the outer sill and shallow inner sill will be referred to as the outer basin, while the basin between the two inner sill will be referred to as the intermediate basin, and finally the basin landward of the deep inner sill as the inner basin. Between the two inner sills the fjord makes a 90° bend in the westerly direction. This bend will be important for observations of propagating internal waves that will be presented in Chapter 3.

Cold water from the St. Lawrence Estuary at the mouth coupled with freshwater supplied by the Saguenay River at the head results in a strongly stratified fjord (Stacey and Gratton, 2001). The water column in the summer exhibits two layer stratification with a 10 m to 20 m thick surface layer of density anomaly ranging from $\sigma_t = 0 \text{ kg m}^{-3}$ near the head to $\sigma_t = 10 \text{ kg m}^{-3}$ near the mouth with a bottom layer of $\sigma_t = 23 \text{ kg m}^{-3}$. The M_2 tidal constituent is most important to the fjord with an amplitude of 1.527 m at the mouth, followed by the S_2 constituent with an amplitude of 0.417 m (Bélanger, 2003).

Stacey and Gratton (2001) used a two-dimensional hydrostatic model to study the influence of the M_2 tide on the circulation of the Saguenay Fjord. They found that the M_2 tide is more intense in the outer basin than in the inner basin, and that there is more mixing in the outer basin. This results in the density at depth decreasing faster in the outer basin and this horizontal density gradient forces deep water from the inner basin to the outer basin via the shallow inner sill.

Bélanger (2003) used a three-dimensional hydrostatic model to examine the dynamics of renewal events in the Saguenay Fjord. He also found a horizontal density gradient existed that opposed the tidal flow caused by the occurrence of deep water rising over the shallow inner sill along with a decrease in density in the outer basin. It is important to note that even if the initial setup of the simulation is two-dimensional there are certain instabilities which develop in three dimensions causing

more turbulent flow and contributing to mixing (Afanasyev and Peltier, 1998).

The details of the nonhydrostatic nature of the flow and high-frequency internal waves around the shallow inner sill have not been examined previously despite the suspected importance of this sill on the overall circulation of the fjord. This motivated this thesis research.

1.3 Objectives

The objective of this thesis is to examine sill processes, in particular internal waves near the shallow inner sill of the Saguenay Fjord. Through numerical simulations (Chapter 2) and a field sampling campaign that took place in the summer of 2007 (Chapter 3) the goal is to gain a better understanding of internal waves in the fjord.

Chapter 2

Simulations

2.1 Introduction

There are no published field observations reporting internal waves in the Saguenay Fjord and previous numerical simulations (Stacey and Gratton, 2001; Bélanger, 2003) were too coarse and used hydrostatic physics to resolve the motion. Processes such as internal waves, internal hydraulic jumps and shear instabilities are nonhydrostatic since the vertical scale of motion is comparable to the horizontal scale. In this chapter, internal waves and sill processes are investigated with the help of high-resolution, non-hydrostatic numerical simulations. Here the analysis is concentrated only near the shallow inner sill to make the simulations computationally efficient.

2.2 Methods

2.2.1 Model

The numerical model used for these simulations is the free-surface, laterally averaged non-hydrostatic model described in Bourgault and Kelley (2004) which solves the

momentum equations

$$\frac{\partial(Bu)}{\partial t} + \frac{\partial(Bu^2)}{\partial x} + \frac{\partial(Buw)}{\partial z} = -\frac{B}{\rho_0} \frac{\partial p}{\partial x} + \frac{\partial}{\partial x} \left(BA_H \frac{\partial u}{\partial x} \right) + \frac{\partial}{\partial z} \left(BA_V \frac{\partial u}{\partial z} \right) - S_f u |u|, \quad (2.1)$$

and

$$\frac{\partial(Bw)}{\partial t} + \frac{\partial(Buw)}{\partial x} + \frac{\partial(Bw^2)}{\partial z} = -\frac{B}{\rho_0} \frac{\partial p}{\partial z} + B \frac{\rho}{\rho_0} g + \frac{\partial}{\partial x} \left(BA_H \frac{\partial w}{\partial x} \right) + \frac{\partial}{\partial z} \left(BA_V \frac{\partial w}{\partial z} \right), \quad (2.2)$$

along with the continuity equation

$$\frac{\partial(Bu)}{\partial x} + \frac{\partial(Bw)}{\partial z} = 0, \quad (2.3)$$

the density equation

$$\frac{\partial(B\rho)}{\partial t} + \frac{\partial(u\rho)}{\partial x} + \frac{\partial(w\rho)}{\partial z} = \frac{\partial}{\partial x} \left(BK_H \frac{\partial \rho}{\partial x} \right) + \frac{\partial}{\partial z} \left(BK_V \frac{\partial \rho}{\partial z} \right), \quad (2.4)$$

and the tracer equation

$$\frac{\partial(BC)}{\partial t} + \frac{\partial(uC)}{\partial x} + \frac{\partial(wC)}{\partial z} = \frac{\partial}{\partial x} \left(BK_H \frac{\partial C}{\partial x} \right) + \frac{\partial}{\partial z} \left(BK_V \frac{\partial C}{\partial z} \right), \quad (2.5)$$

where x is the horizontal coordinate with its origin centered on the shallow inner sill and positive seaward; z is the vertical coordinate with its origin at the undisturbed sea surface and positive downward; $B(x, z)$ is the varying width (see Figure 2.1); $u(x, z, t)$ is the horizontal velocity component; $w(x, z, t)$ is the vertical velocity component; $p(x, z, t)$ is the pressure; ρ_0 is a constant reference density; g is gravitational acceleration, and S_f is a side friction coefficient given by

$$S_f = S_0 \left(1 + \left| \frac{dB}{dz} \right| \right), \quad (2.6)$$

where $S_0 = 0.003$. The eddy viscosity A_H , A_V , and diffusivity K_H , K_V are parameterized using the Smagorinsky (1963) scheme as presented in Bourgault and Kelley (2004).

C is a passive tracer initially set to be a linear function of the depth z ,

$$C(x, z, t = 0) = z \quad (2.7)$$

The tracer has no physical significance and does not impact the model outputs. It is used as a visual aid as it shows the motion of the water at all depths whereas density would only provide visual information near the pycnocline.

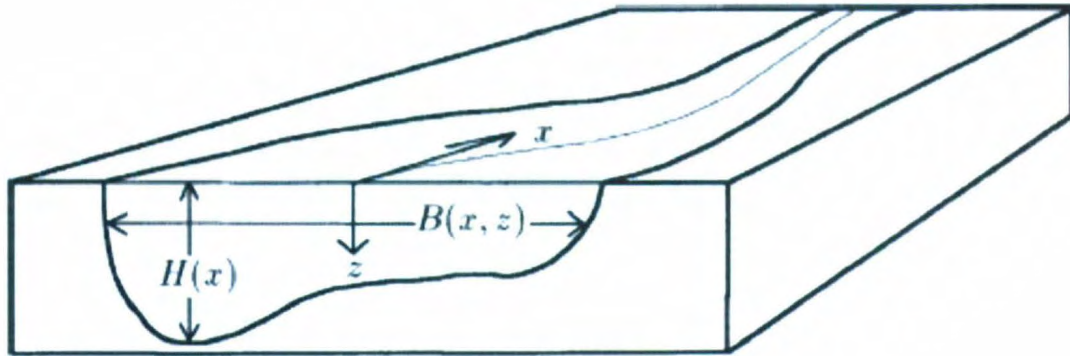


Figure 2.1: Schematic diagram of the model geometry (From Bourgault and Kelley, 2004)

A bathymetry file of the Saguenay Fjord was created by digitizing Canadian Hydrographic Service nautical charts 1202 and 1203. Using this bathymetry file a digital data set containing latitude, longitude, and corresponding depths and widths of the fjord was created.

The model has a gridded structure which allows the user to have higher resolution in areas of greater interest. A stretch factor of 1.1 is used to increase the size of each consecutive cell away from the area of high resolution to make the simulation computationally efficient.

This research is concerned with processes around sills so the area around the shallow inner sill is where the simulation has highest resolution. The finest horizontal resolution occurs at 2000 m on each side with a value of $\Delta r_{\min} = 3.5$ m, increasing to $\Delta r_{\max} = 1000$ m farther away (Figure 2.2). In the horizontal $\Delta z_{\min} = 1$ m in the first 160 m, increasing to $\Delta z_{\max} = 10$ m thereafter (Figure 2.3).

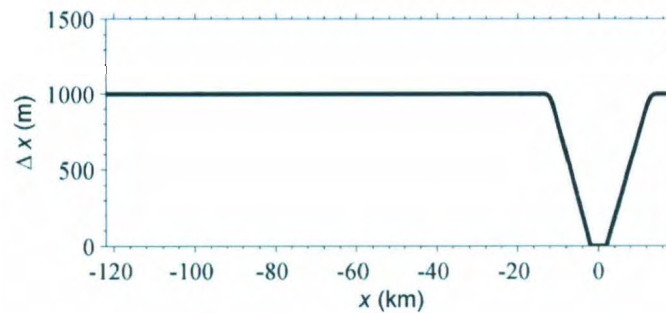


Figure 2.2: Horizontal resolution. The grid size is $\Delta r_{\min} = 3.5$ m 2000 m on each side of the sill, increasing by a stretch factor of 1.1 to $\Delta r_{\max} = 1000$ m.

Interpolating the digitized bathymetry data onto the numerical grid produces files which are then used to initialize the model. Figure 2.4 shows the varying width and depth of the fjord used for the simulations. The area around the shallow inner sill has noticeably finer resolution when compared to areas in the long basin.

The model is forced at the seaward boundary using the M2 tidal constituent which has a period of 12.42 hours and an amplitude of 1.527 m at Tadoussac (Bélanger, 2003). To simulate the freshwater influx at the head of the fjord from the Saguenay

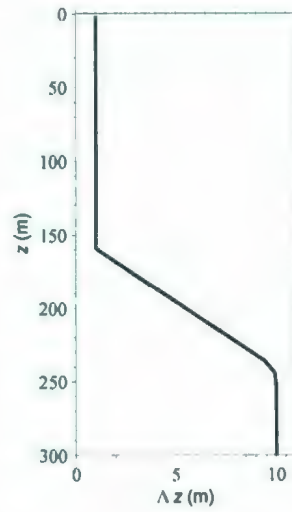


Figure 2.3: Vertical resolution. The grid size is $\Delta z_{\min} = 1$ m for the first 160 m of depth, increasing by a stretch factor of 1.1 to $\Delta z_{\max} = 10$ m.

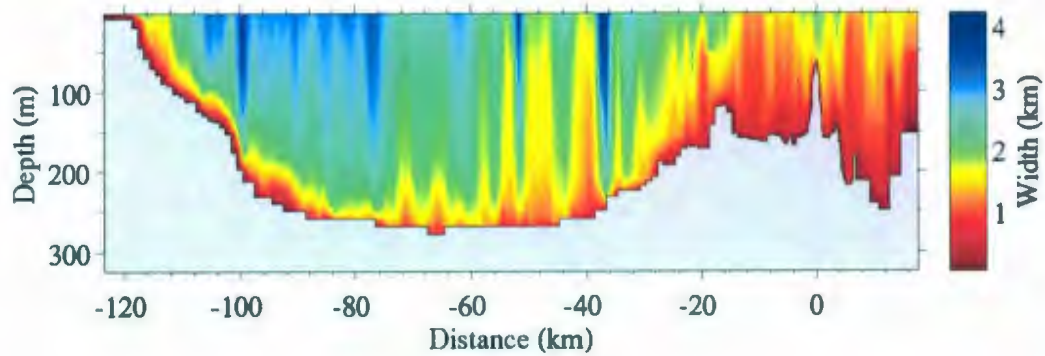


Figure 2.4: Width $B(x, z)$ and depth $H(x)$ of the fjord interpolated on a variable grid with maximum horizontal resolution ($\Delta x_{\min} = 3.5$ m) centered around the inner sill (i.e. at $x = 0$).

River a value of $1200 \text{ m}^3 \text{ s}^{-1}$ is imposed (Stacey and Gratton, 2001).

Two cases will be examined in this thesis, an unstratified case in which the initial density profile is constant at 1017.5 kg m^{-3} , and a stratified case where the initial density profile is longitudinally uniform and vertically takes the functional form

$$\rho = \rho_1 + \frac{\Delta\rho}{2} \left(1 + \tanh \left[\frac{z - z_i}{\Delta h} \right] \right), \quad (2.8)$$

where $\rho_1 = 1010 \text{ kg m}^{-3}$, $\Delta\rho = 14.5 \text{ kg m}^{-3}$, $\Delta h = 2 \text{ m}$, and $z_i = 10 \text{ m}$ (Figure 2.5).

The corresponding buoyancy frequency, N , is calculated by

$$N = \left(\frac{g \partial \rho}{\rho \partial z} \right)^{\frac{1}{2}} \quad (2.9)$$

The simulations were run on the Atlantic Computational Excellence Network (ACEnet) allowing for more than one simulation to be running at a given time.

2.2.2 Analysis

Visually, from images and animations of the outputs, both internal waves and overturning events can be seen. However, this only gives a qualitative analysis of the simulation. In an effort to quantify the results, calculations were carried out with regard to the kinetic energy of the system.

A one hour moving average filter is used to perform a Reynold's decomposition on the horizontal velocity u , and the vertical velocity w separating the instantaneous timeseries into the mean signal and fluctuation denoted by $\langle u \rangle$ ($\langle w \rangle$) and u' (w'), respectively,

$$\begin{aligned} u &= \langle u \rangle + u', \\ w &= \langle w \rangle + w'. \end{aligned} \quad (2.10)$$

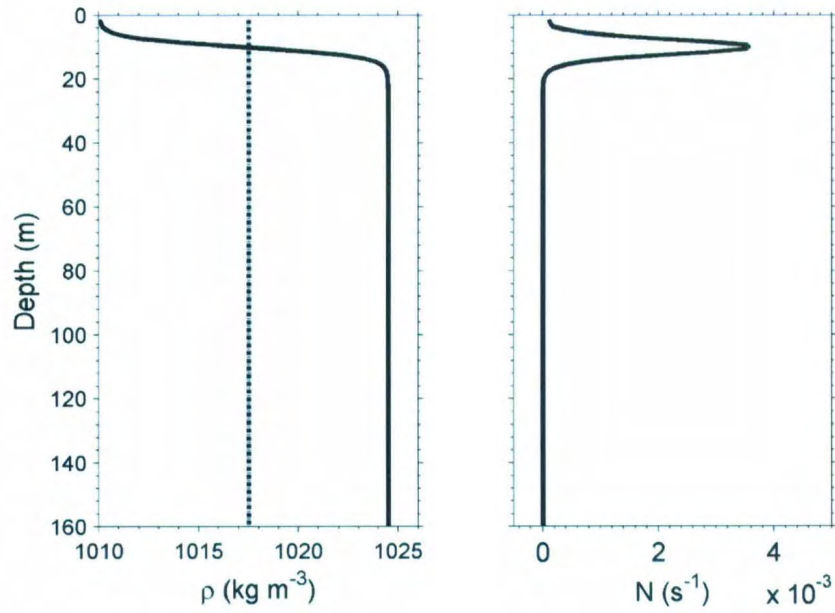


Figure 2.5: The left panel shows the density profile used for the stratified case (solid) and the unstratified case (dotted). The right panel shows the corresponding buoyancy frequency for the stratified case.

The spatial intensity of the kinetic energy associated with sill processes is determined as

$$K'(x, z) = \frac{1}{2} \rho_o \left(\overline{u'^2} + \overline{w'^2} \right) B \quad [\text{J m}^{-2}] \quad (2.11)$$

where, $\rho_o = 1010 \text{ kg m}^{-3}$. This provides the field which one would expect to find high-frequency sill processes such as internal waves and turbulence.

Knowing where, on average, the maximum fluctuation in kinetic energy occurs is one step toward better understanding the processes around the shallow inner sill of the Saguenay Fjord. However, the intensity of the kinetic energy changes throughout a tidal cycle as well. The temporal variability of the kinetic energy is estimated using,

$$K'_t(t) = \int_{z_\eta}^{z_H} \int_{x_{\min}}^{x_{\max}} \frac{1}{2} \rho (u'^2 + w'^2) B dx dz \quad [\text{J}], \quad (2.12)$$

where η is the surface elevation and ρ is the density. In the horizontal, the high resolution area is divided into a landward and seaward side (Figure 2.6) at the x -origin resulting in $x_{\min} = -2000(0) \text{ m}$ and $x_{\max} = 0(2000) \text{ m}$ for the landward (seaward) side. Treating each side of the sill independently allows for comparisons to be made as one would expect activity on each side of the sill to differ throughout a tidal cycle. For example, when one side of the sill is turbulent and subject to breaking waves, the other side is quiet and laminar and vice-versa at the opposite phase of the tide (see for example Figures 1.1 and 1.2).

Using the resolution depicted in Figures 2.2 and 2.3 the model was ran for five simulated days in both the stratified and unstratified cases. To give the model time to stabilize the initial semi-diurnal tidal cycle is not included in any calculations.

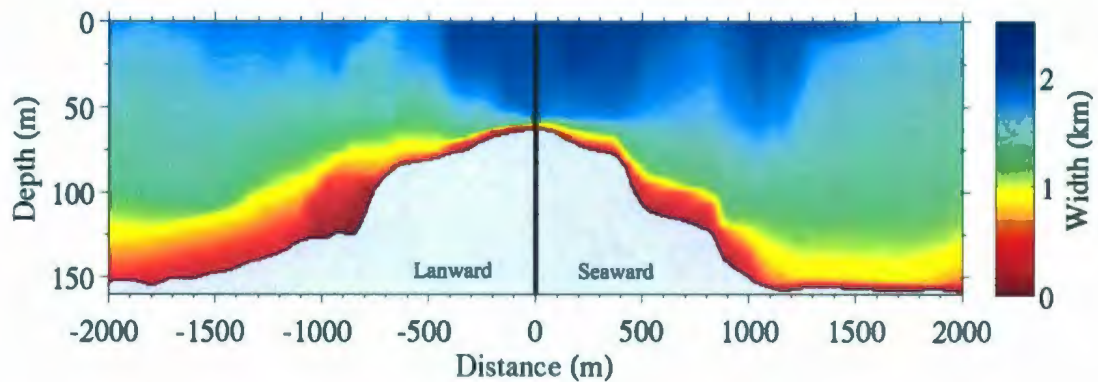


Figure 2.6: Details of the depth and width around the inner sill where maximum resolution ($\Delta x = 3.5$ m) is used. The vertical black line delimits the two regions on each side of the sill where the temporal variations of the kinetic energy (see Equation 2.12) is calculated.

2.3 Results

2.3.1 Flow structure

Figures 2.7 and 2.8 show the progression of the flow using the passive tracer C about the sill throughout one semi-diurnal tidal cycle for the unstratified and stratified cases, respectively.

In both figures we see a lot of activity on each side of the sill and evidence that while one side has turbulent flow the other side's flow is more laminar (see panels $\tau = 0.00, 4.05, 11.37,$ and 12.40 h in Figure 2.7 and panels $\tau = 0.00, 1.20, 10.20,$ and 12.40 h in Figure 2.8). Looking at all the panels in Figure 2.8 it is seen that above 10 m depth there is little turbulent activity. Qualitatively, the simulations suggest that the pycnocline is acting like a barrier preventing vertical velocities above it. By comparison, in Figure 2.7 turbulent activity is occurring throughout the entire water

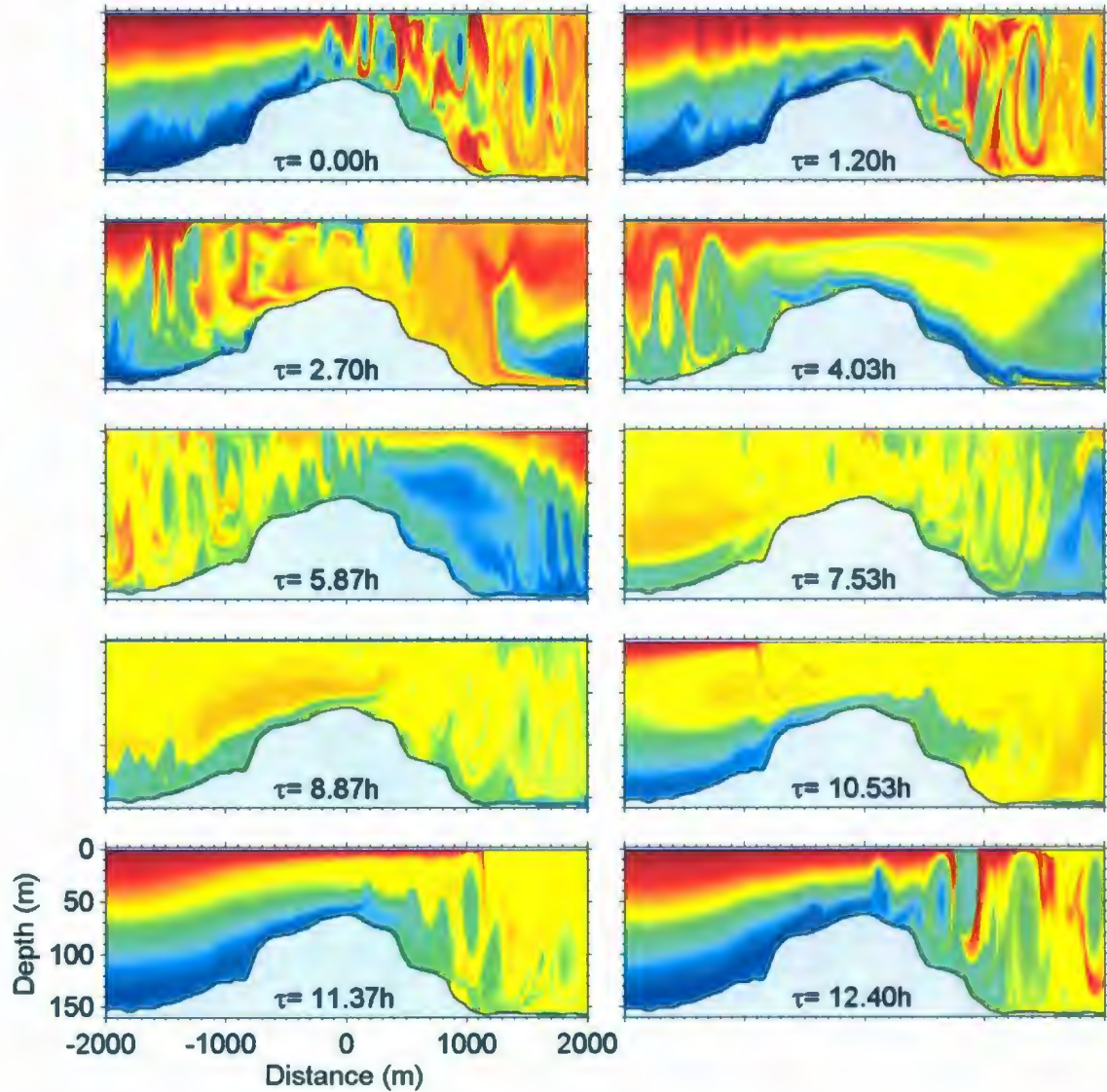


Figure 2.7: Images show the progression of tidal flow for the unstratified case using the passive tracer C . τ is the time in hours with respect to low water at Tadoussac with $\tau = 0$ being at the low water mark. The passive tracer is only used for visualization with the units being arbitrary.

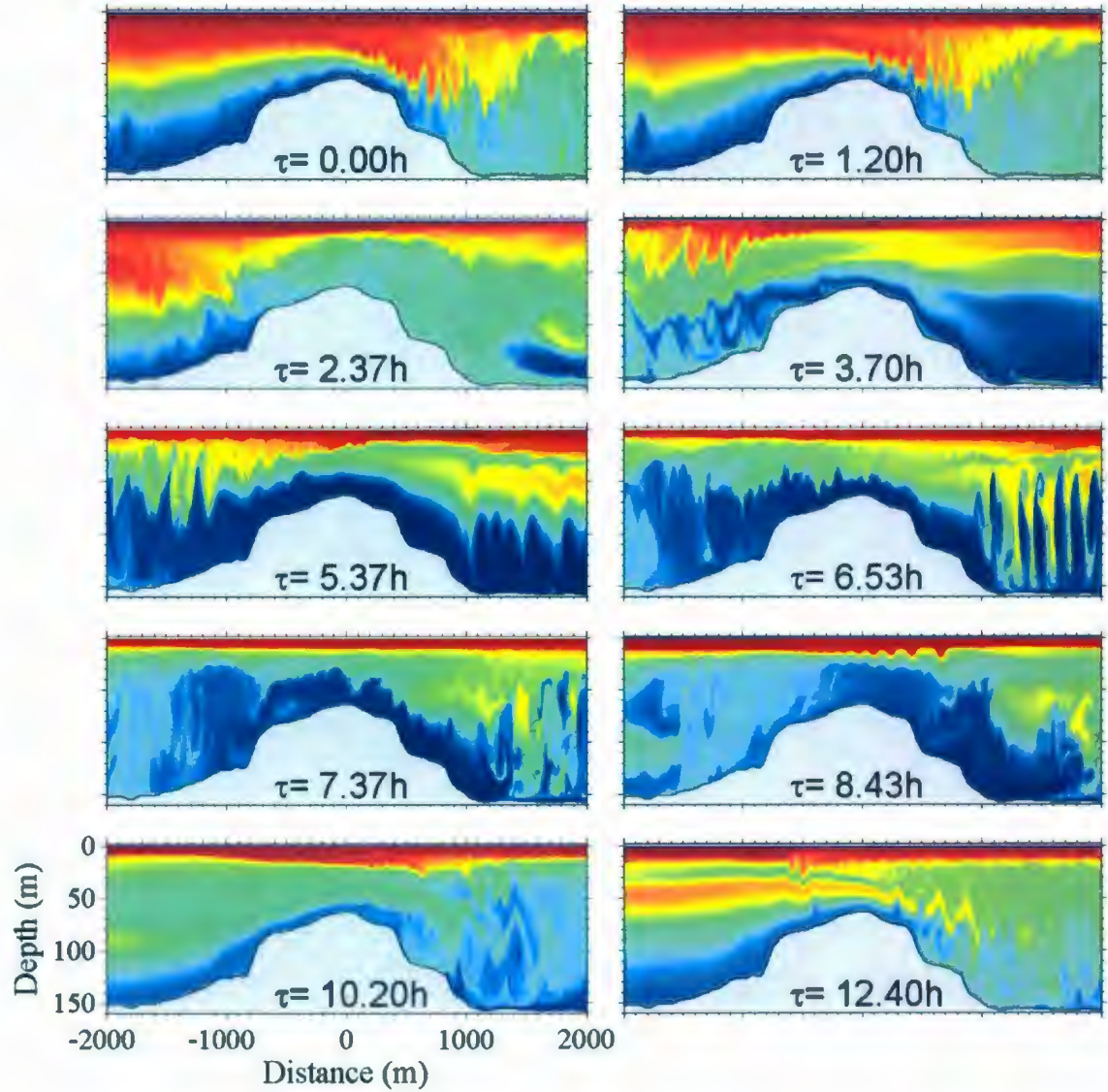


Figure 2.8: Images show the progression of tidal flow for the stratified case using the passive tracer C .

column, and by panel $\tau = 7.53$ h areas on each side of the sill are almost uniformly mixed.

Taking a closer look at panels $\tau = 0.00, 5.87,$ and 12.40 h in Figure 2.7 and panels $\tau = 0.00, 5.37,$ and 12.40 h in Figure 2.8 we see that the side of the sill which is more turbulent switches as the tidal flow reverses about every 6 hours.

Large-scale eddies on the order of 125 m in height can be seen in panel $\tau = 1.20$ h of Figure 2.7 almost encompassing the entire water column. These eddies grow so large since there is no stratified layer to restrict them. Between 75 m and 125 m depth on the landward side of panels $\tau = 0.00,$ and 1.20 h we also see evidence of Kelvin-Helmholtz instabilities.

Concentrating on the stratified case we again see very large eddies on the order of 100 m amplitude being advected from one side to the other ($\tau = 5.37$ h to $\tau = 6.53$ h). Since the initial density profile is essentially two layered there is little stratification in the lower water to restrict the growth of these overturns. In reality, the bottom layer is slightly stratified (not shown here) and these eddies are probably limited in size by the stratification in the deep bottom layer.

The corresponding horizontal and vertical velocities for the stratified case can be seen in Figures 2.9 and 2.10, respectively. In panel $\tau = 3.70$ h of Figure 2.9 the horizontal flow on the landward side of the sill exhibits a three layer structure in which a 50 ± 5 m thick intermediate layer is seen flowing landward while the top and bottom layers are flowing seaward. The reverse of this is seen in panel $\tau = 10.20$ h on the seaward side with a 45 ± 5 m intermediate layer flowing seaward with the top and bottom layers flowing landward.

Clearly validates in all panels that when one side of the sill is turbulent the other side is far quieter (Figure 2.10). The overturns are also visible in this figure by the banded nature of the vertical velocity.

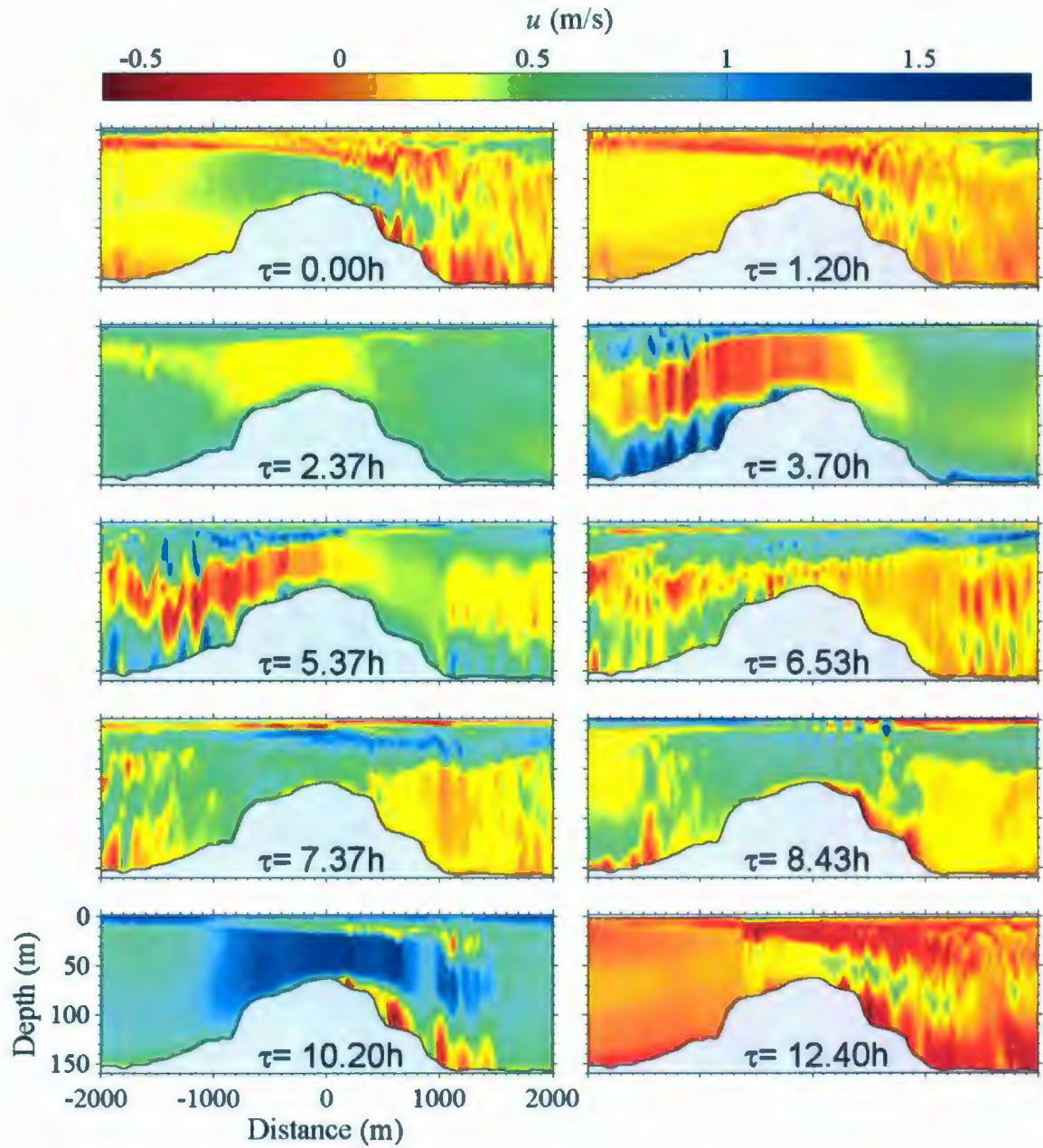


Figure 2.9: Images show the progression of tidal flow in the stratified case using u .

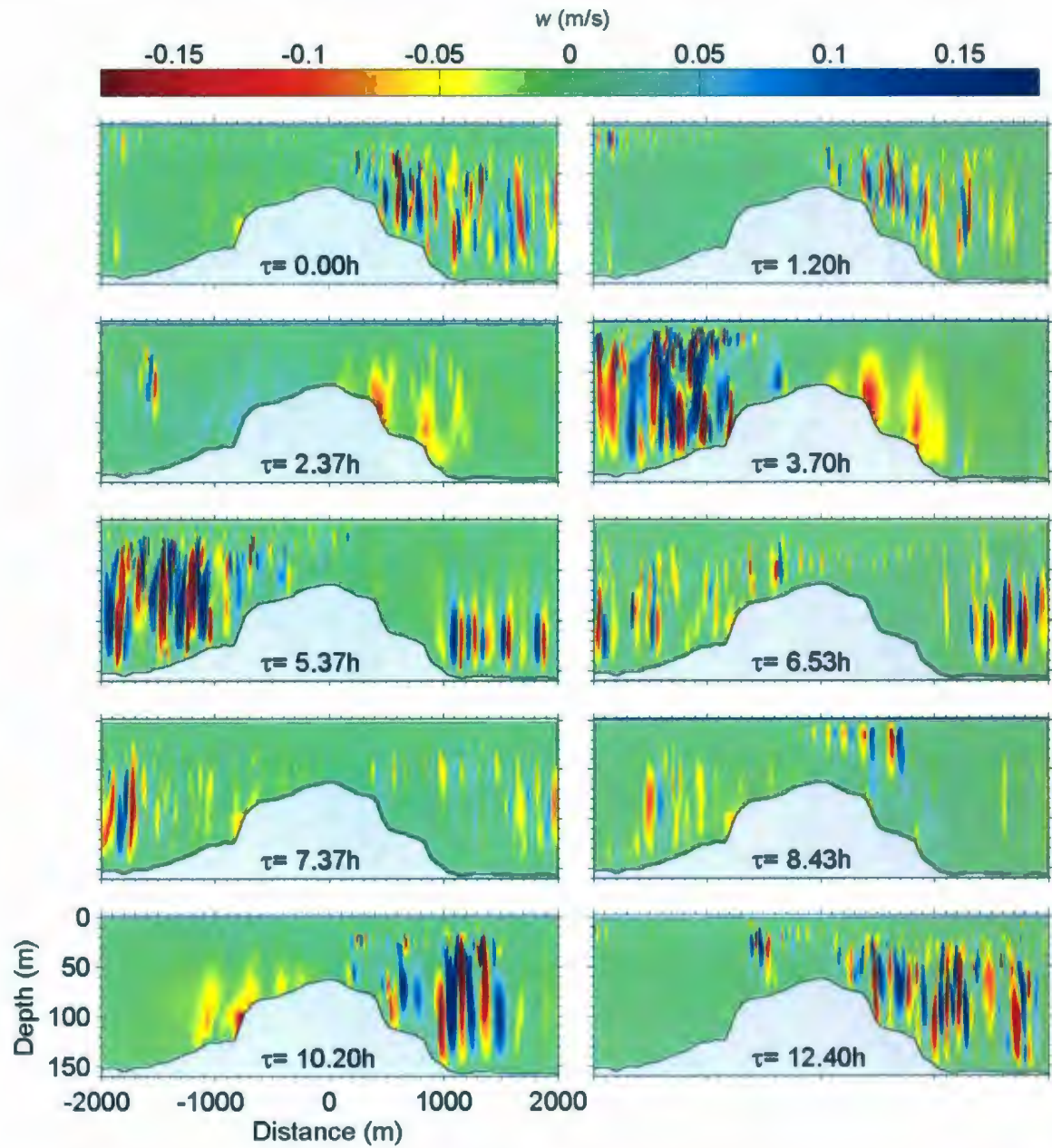


Figure 2.10: Images show the progression of tidal flow in the stratified case using w .

A close look at the top portion of panel $\tau = 8.43$ h in both Figures 2.8 and 2.10 shows the presence of an internal wavetrain. An enlargement of this wavetrain is shown in Figure 2.11. The amplitude of this wavetrain is $a = 8(5, 12)$ m, where the numbers in parentheses represent the smallest and largest values, and the wavelength of this train is $L = 170(120, 235)$ m. This wavetrain is typical of a solitary wavetrain with the waves exhibiting a sech^2 structure and with the waves ranked ordered in amplitude. Many other similar wavetrains appear to be generated around the sill throughout the simulation (not shown here but clear from animations).

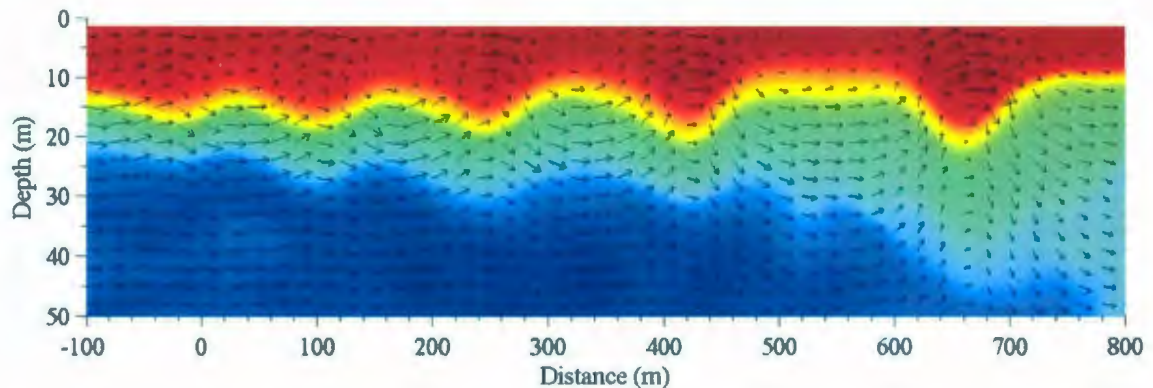


Figure 2.11: Internal wavetrain propagating seaward at $\tau = 8.43$ h. For plotting the vectors the mean horizontal current has been removed.

2.3.2 Kinetic Energy

An example of the Reynold's decomposition for the stratified case that was performed on a cell located at $x = 1251$ m and $z = 31$ m can be seen in Figure 2.12. The fluctuations appear mostly during flood tide and have magnitudes of up to 0.5 m s^{-1} .

Using Equation 2.11 for both the stratified and unstratified cases the spatial intensity of the kinetic energy was calculated (Figure 2.13). The color scale has been

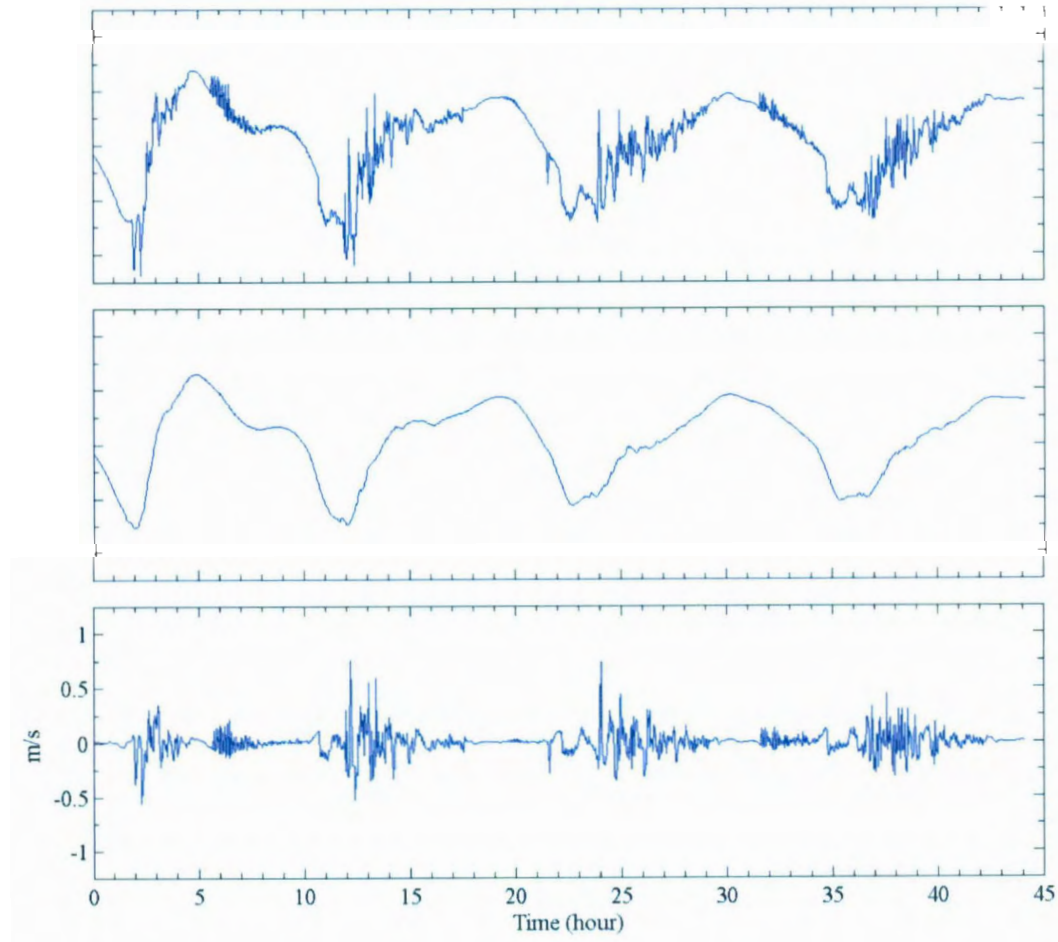


Figure 2.12: Example of Reynold's decomposition on a cell located at $x = -1251$ m, $z = 31$ m. The top panel is u , the middle panel is $\langle u \rangle$ and the bottom panel is u' .

forced the same so that direct comparisons can be made between figures.

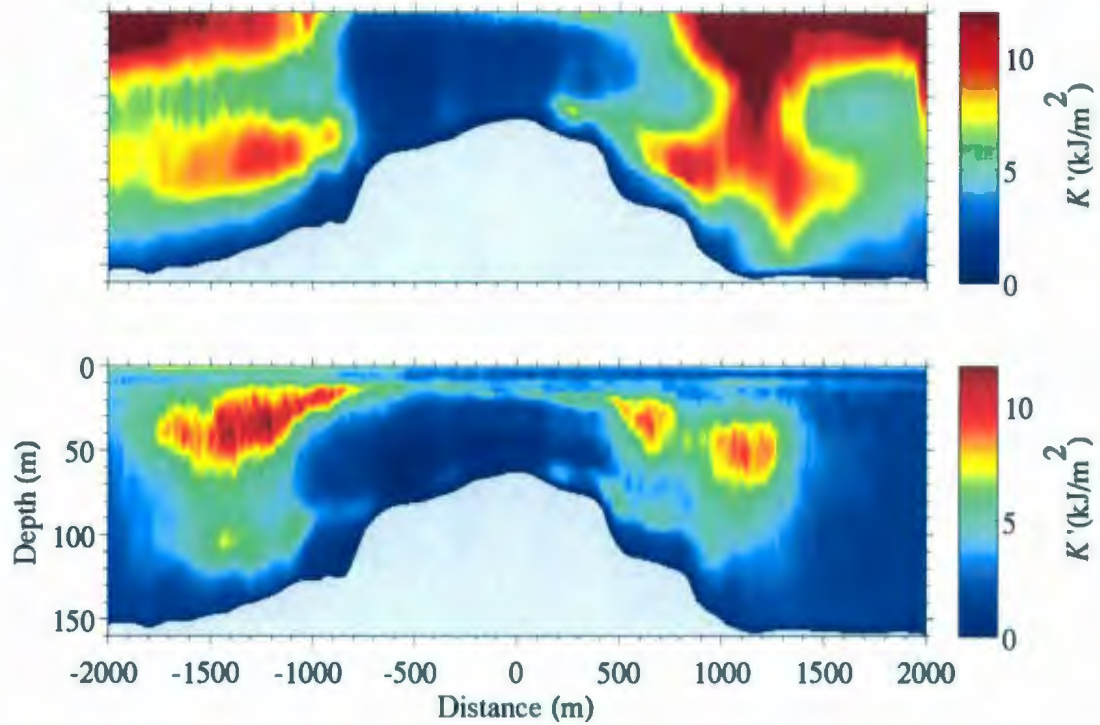


Figure 2.13: Fluctuation from mean kinetic energy for the stratified (bottom) and unstratified (top) cases. The color scales have been forced to be the same.

Figure 2.13 quantifies the qualitative assertions made in the previous section that in both the stratified and unstratified cases the areas on each side of the sill are most active. Looking at the stratified case, we see that there are two hot spots for turbulence, on the landward side at $-1700 < x < -900$ m, $10 < z < 50$ m and on the seaward side at $600 < x < 1200$ m, $20 < z < 60$ m. The center of these regions produce kinetic energy values on the order of approximately 10 kJ m^{-2} with the landward side having a maximum kinetic energy of about 2 kJ m^{-2} greater than the seaward side.

The barrier at the 10 m pycnocline is visible in the stratified case with the kinetic energy below being nearly an order of magnitude higher than that above, while in the unstratified case the spatial intensity of kinetic energy is not bounded and high rates are observed near the surface.

A timeseries was created using Equation 2.12 (Figure 2.14). Averages over three semi-diurnal tidal cycles were used and the values are plotted with respect to low water in Tadoussac.

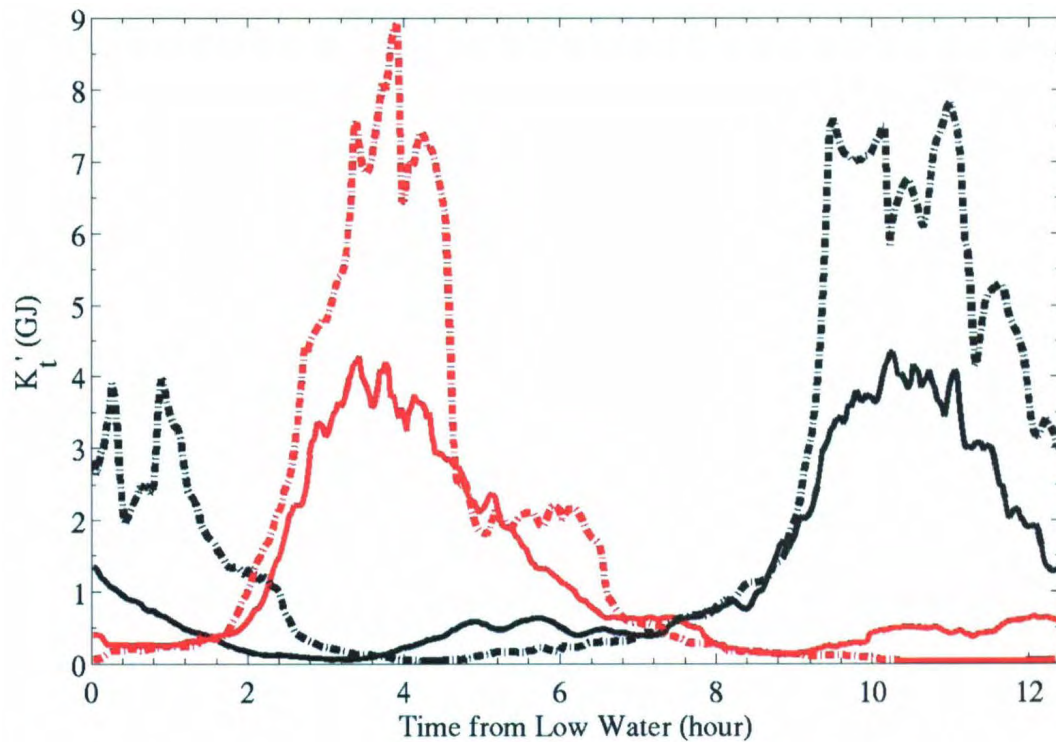


Figure 2.14: Timeseries of total fluctuation from the mean kinetic energy for the stratified (solid) and unstratified (dotted) simulations. Red corresponds to the landward side of the sill while black is for the seaward side.

Figure 2.14 provides insight into the timing of maximum kinetic energy fluctuation on each side of the sill. The timing of the peak fluctuation for both the stratified and unstratified cases agree within one hour on each side of the sill, occurring between 3.5 to 4.5 hours after low water on the landward side and between 9.5 and 10.5 hours after low water on the seaward side.

The intensity of the maximum fluctuation in the unstratified case is more than double that experienced in the stratified one on both sides of the sill. Maximum values on the landward (seaward) side of the sill in the unstratified case are approximately 9 (7.5) GJ, compared to about 4.5 GJ on both sides of the sill in the stratified case. This is to be expected as stratification restricts movement in the water column.

2.4 Discussion

Results here show that both sides of the shallow inner sill of the Saguenay Fjord experience turbulent activity and the existence of large-scale eddies and internal waves. The patterns simulated here are similar to observations (Figure 2.15) of turbulent dissipation rates near the sill in Knight Inlet (Klymak and Gregg, 2003) who found very high rates near the sill, while away from the sill the rates were significantly lower.

The information provided by these results can be quite useful in planning field experiments as Figures 2.13 and 2.14 provide insight as to where and when one might expect to see processes such as turbulent mixing or internal wave generation. As well, animations of the tidal flow can provide more specific regions to sample.

The two-dimensionality of the simulations limits the results as it cannot account for cross-channel motion. This limits accuracy as it has been shown in similar environments that the flow around a sill can be quite three dimensional (Klymak and Gregg, 2001; Baker and Pond, 1995). During their experiment, Klymak and Gregg

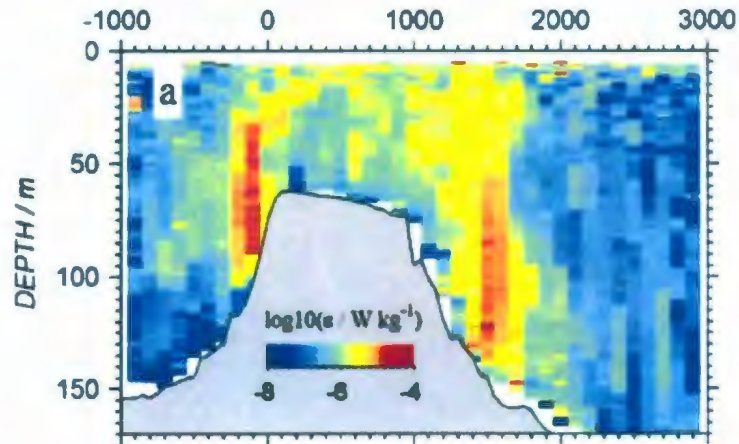


Figure 2.15: Field observations from Klymak and Gregg (2003) showing the turbulent dissipation rate near the sill in Knight Inlet. Landward is positive on the x-axis.

expected the flow around the sill to be two dimensional but instead found strong three dimensional flow during both phases of the tide.

These results show the limitations of using a two dimensional simulation to understand the flow around a sill. That being said, such a simplified model does still provide valuable insight.

Chapter 3

Field Observations

3.1 Introduction

The simulations were used to aid in planning a field study of the Saguenay Fjord, in particular the area around the shallow inner sill. The initial planning for location and timing of sampling was mostly based on Figures 2.13 and 2.14 since there does not exist a lot of literature on internal waves in the Saguenay Fjord.

This chapter will examine the results of the field study beginning with sampling strategy and some data analysis, followed by a closer look at a large amplitude internal wavetrain and evidence of internal wave reflection.

3.2 Methods

3.2.1 Sampling

The field location was centered around the shallow inner sill of the fjord (Figure 3.1) with sampling carried out over seven non-consecutive days between July 1st and 14th, 2007.

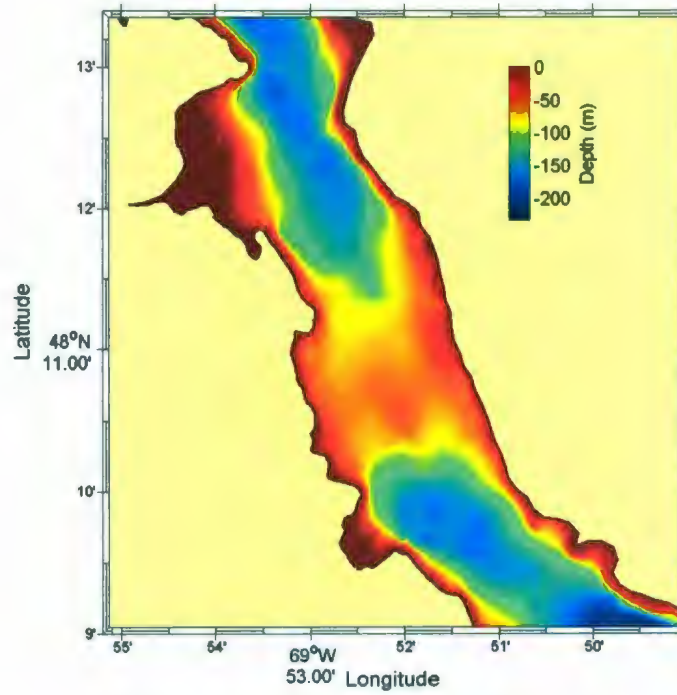


Figure 3.1: Zoom of the shallow inner sill of the Saguenay Fjord. Location for the field study presented in this chapter.

Sampling was conducted from an eight meter long Canadian Coast Guard boat, the Krill, which allowed for quick access to the areas of interest. It was fitted with a GPS which logged the location of the boat at five second intervals. A downward looking 600 KHz RDI Workhorse Acoustic Doppler Current Profiler (ADCP) which collected three-dimensional current and backscatter intensity data was used. The pinging rate of the ADCP was 1.25 Hz, recording 5 second ensemble averages in 0.25 m vertical bin size. As well, a free-falling, loosely tethered Rockland Scientific Vertical Microstructure Profiler (VMP) collected fine-scale pressure, temperature, conductivity and microscale vertical shear. The VMP was retrieved using a drill powered winch.

In addition, for five of the seven days a scientist located on a nearby hill with a Canon Power Shot S70 digital camera took pictures in one minute intervals for the duration of the study. This provided simultaneous data collection from the Krill and time-lapse photography of sea-surface patterns.

The majority of the observations were concentrated on the landward side of the sill. The main reason for this was that accessible hills for setting the camera were only found to provide good field of views of the water on this side of the sill.

With respect to timing, an effort was made early on to follow the information provided by the simulation results presented in the previous chapter (e.g. Figure 2.14). However, these times did not always occur during daylight, thus negating the use of the camera. Sampling generally started in the morning and continued until late afternoon resulting in being on-site for approximately half a semi-diurnal tidal cycle everyday.

The sampling strategy once onsite was to search visually for banded sea surface patterns commonly caused by internal waves (Farmer and Armi, 1999; Bourgault and Kelley, 2003). This process was aided greatly by the cameraman whose elevation

made it much easier to spot the sea surface signature of internal waves. When the cameraman saw a banded sea-surface pattern typical of those induced by internal waves he radioed the Krill and the boat would be re-positioned up-stream of the wave and left to drift.

Once the Krill started drifting the ADCP would be hung over the side at a depth of approximately 0.5 m below the surface and as many VMP profiles as possible were collected.

3.2.2 Data Analysis

The still images obtained from the camera provide an inexpensive data set which is used to further study the flow around the sill. To do this the images need to be first geo-rectified, a process explained by Pawlowicz (2003). The same technique and scripts used for this thesis were tested by Bourgault (2008) for monitoring river ice. For technical details on the implementation of these scripts for this thesis refer to Appendix A.

The ADCP recorded a timeseries of data for the backscatter intensity I , horizontal velocities u and v , and vertical velocity w . Transforming ADCP data from temporally to spatially dependent makes it easier to extract information from that data, such as the wavelength of an internal wave train. However, since sampling was carried out from a boat that was drifting relative to the propagating internal waves the internal waves recorded are Doppler shifted.

The first step required to correct for the Doppler shift is to interpolate the original timeseries ADCP data onto a spatial domain. This is accomplished by using the data from the GPS onboard the Krill.

Taking this recorded position to be x' we can find the position corrected for

Doppler shift (x) by

$$x = x' - c\Delta t \quad (3.1)$$

where c is the phase speed of the wave and Δt is the time with $t = 0$ at $x = 0$. The phase speed of the internal waves is determined from simultaneous georectified photographs of the sea-surface manifestation of internal waves. Without such simultaneous photographs for a given wavetrain the correction for the Doppler shift cannot be applied.

An example of this method, along with validation, is presented in Appendix B.

3.3 Results

In all twenty-three wavetrains were observed using the ADCP. The naming convention used for the wavetrains is alphabetical, A-W. This section will look at some of these wavetrains in greater detail followed by two instances in which internal wave reflection against the lateral boundaries of the fjord will be documented.

3.3.1 A large-amplitude wavetrain

A particularly well defined internal wave train was observed on July 9th. The ability to quickly reposition the boat in front of the train resulted in passing through it four times while at the same time getting still images of the surface. Figure 3.2 shows the boat tracks of the four passes made through the wavetrain.

For tracks G and H, the Krill is drifting more along channel, while in I and J the boat is drifting more onshore. The intent for drifts I and J was to follow the path of G and H, however the current forced the Krill onshore. Figure 3.3 displays the

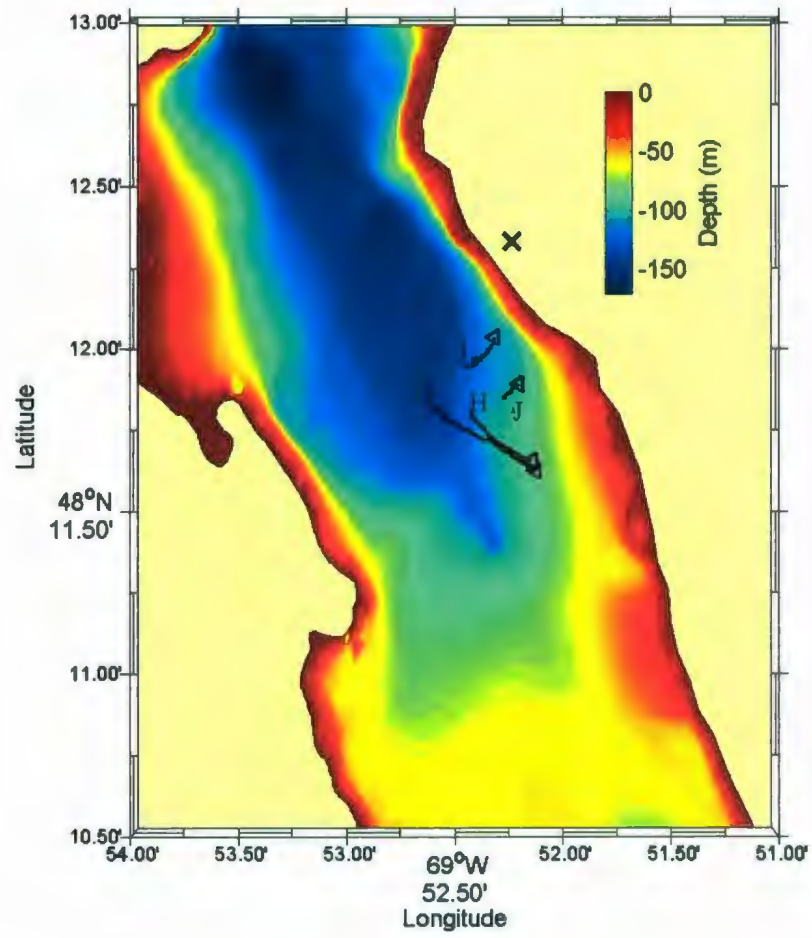


Figure 3.2: GPS tracks for July 9th. The 'X' represents the location of the camera-man.

ADCP backscatter intensity for the four passes G-J.

From pass G to H the internal waves has steepened substantially with increased amplitude and decreased wavelength. A more quantitative analysis of these two wavetrains follows. Passes I and J do not show the same well formed internal wavetrain and it is not certain whether these passes were actually through the same wavetrain. Photographs and GPS data verify that G and H are.

Taking a closer look at trains G and H and their corresponding vertical and horizontal velocities (Figures 3.5 and 3.6, respectively) gives a better depiction of each wavetrain's structure. The wavetrains propagated into a background environment characterized by the density structure shown in Figure 3.4.

In both cases the density exhibits a 2 layer structure with the pycnocline located at approximately 5 m and the density difference between the layer is around $\Delta\rho = 11 \text{ kg m}^{-3}$. The intensity coupled with the banded structure of the vertical velocity in Figures 3.5 and 3.6 shows a strong internal wave signal. Looking at the vertical velocity plots it is clear that from pass G to H the wavetrain has become far more symmetric. It should be noted that the color axis for the velocity plots have been forced to eliminate the presence of outliers.

These wavetrains also produced a strong banded sea surface structure which can be seen in Figure 3.7 and Figure 3.8.

These geo-rectified images show a snapshot of the sea surface signature of the waves, while the ADCP plots provide temporal data. Using the method discussed in the previous section wavetrains G and H have been transformed from temporally to spatially dependent (Figure 3.9).

The ability to sample an internal wavetrain as it propagates provides a lot of information about how that train is evolving. The phase speed, wavelength and peak to trough range can be obtained and compared for each pass. For this thesis, the

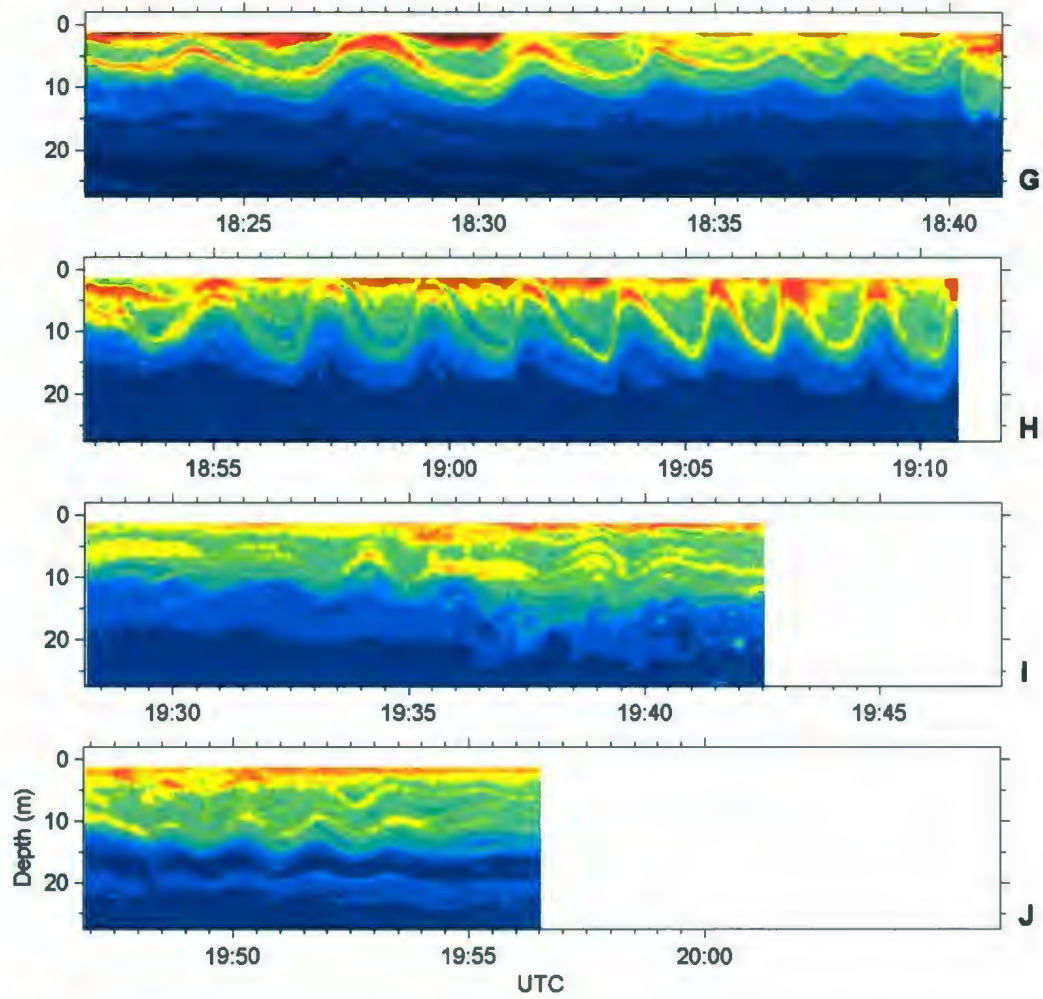


Figure 3.3: Backscatter intensity plots for the four passes made through an internal wave train on July 9th, 2007.

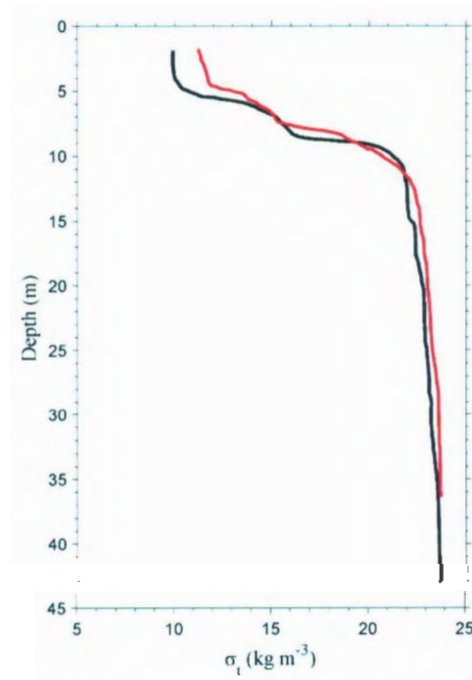


Figure 3.4: Density profiles of the water structure prior to wavetrains G (black) and H (red) passing through.

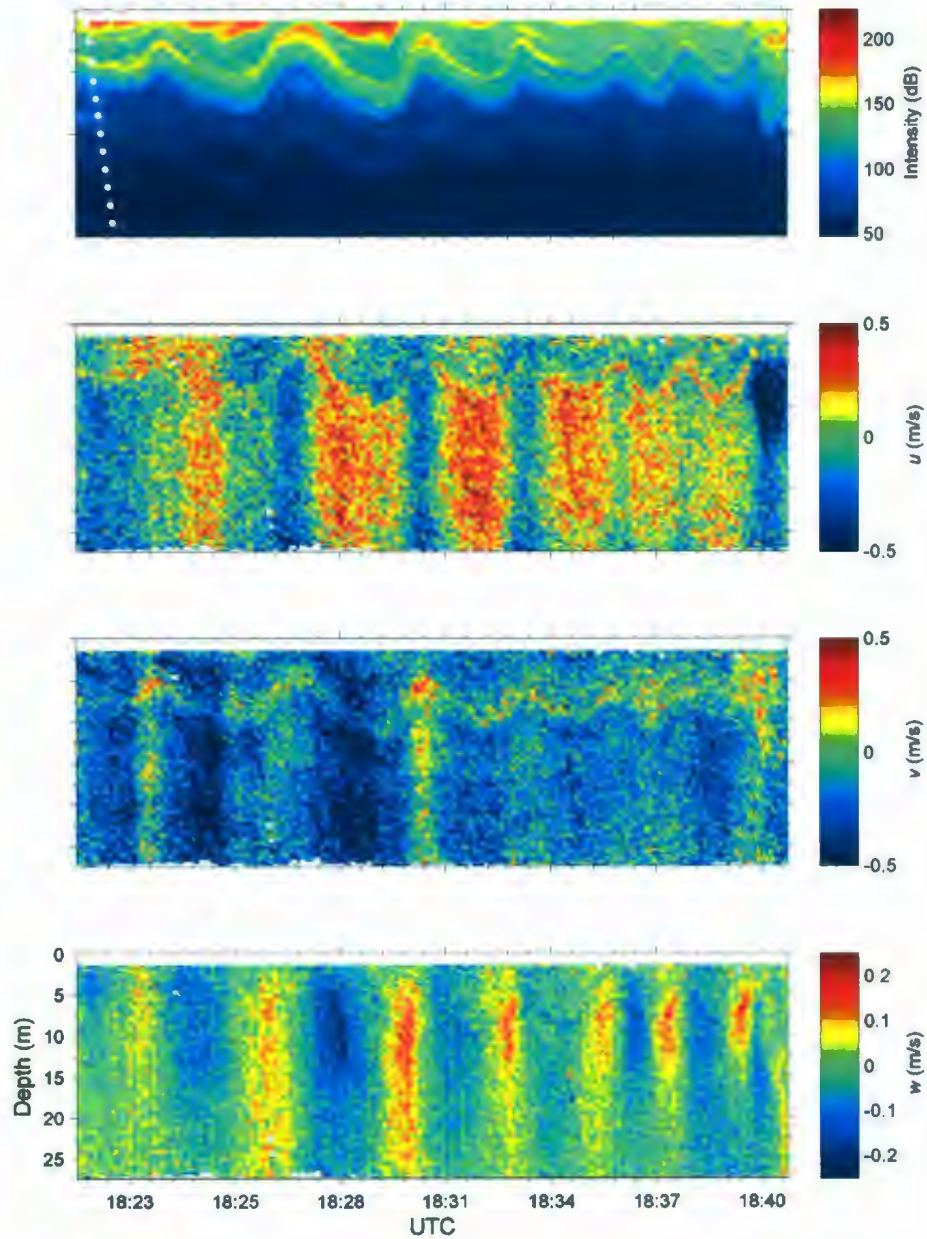


Figure 3.5: Intensity, horizontal velocities u and v , and vertical velocity w for track G on July 9, 2007. The white dotted line in the intensity plot shows the location of the VMP profile used to calculate σ_t displayed in Figure 3.4.

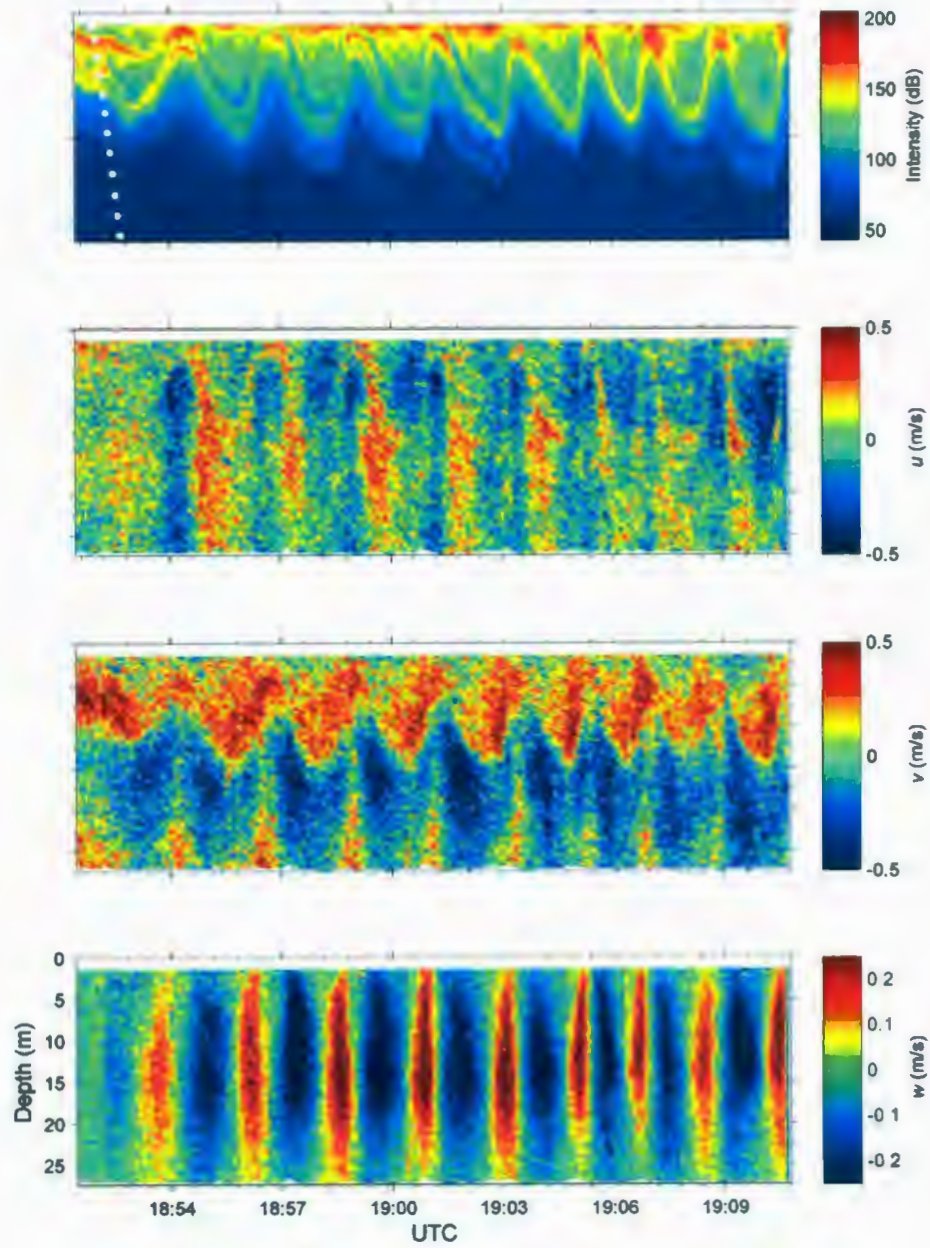


Figure 3.6: Intensity, horizontal velocities u and v , and vertical velocity w for track H on July 9, 2007.

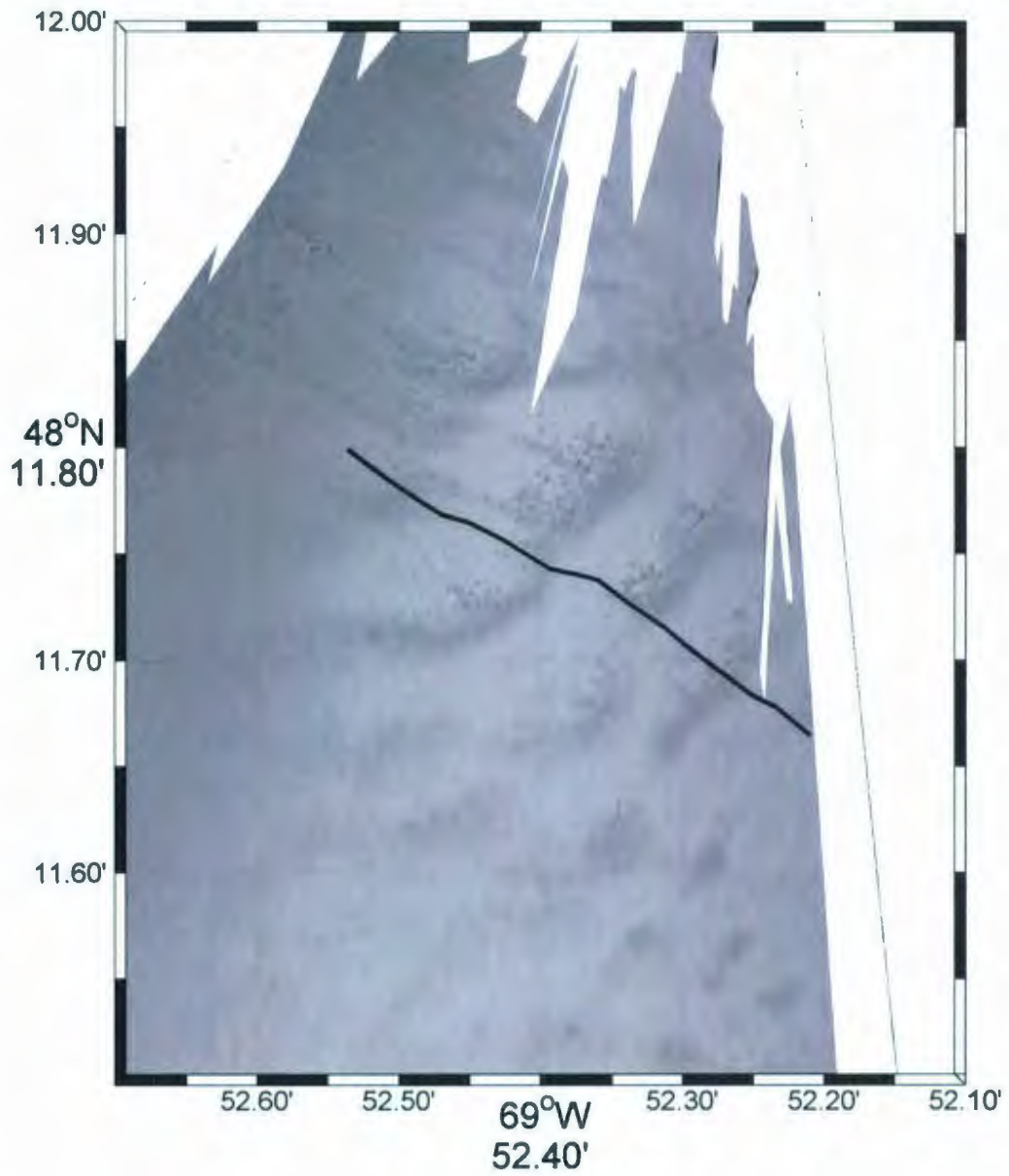


Figure 3.7: Georectification image showing wavetrain G. The black line indicates the GPS track of the Krill, which is out of sight of the camera in this frame, but is still collecting data.

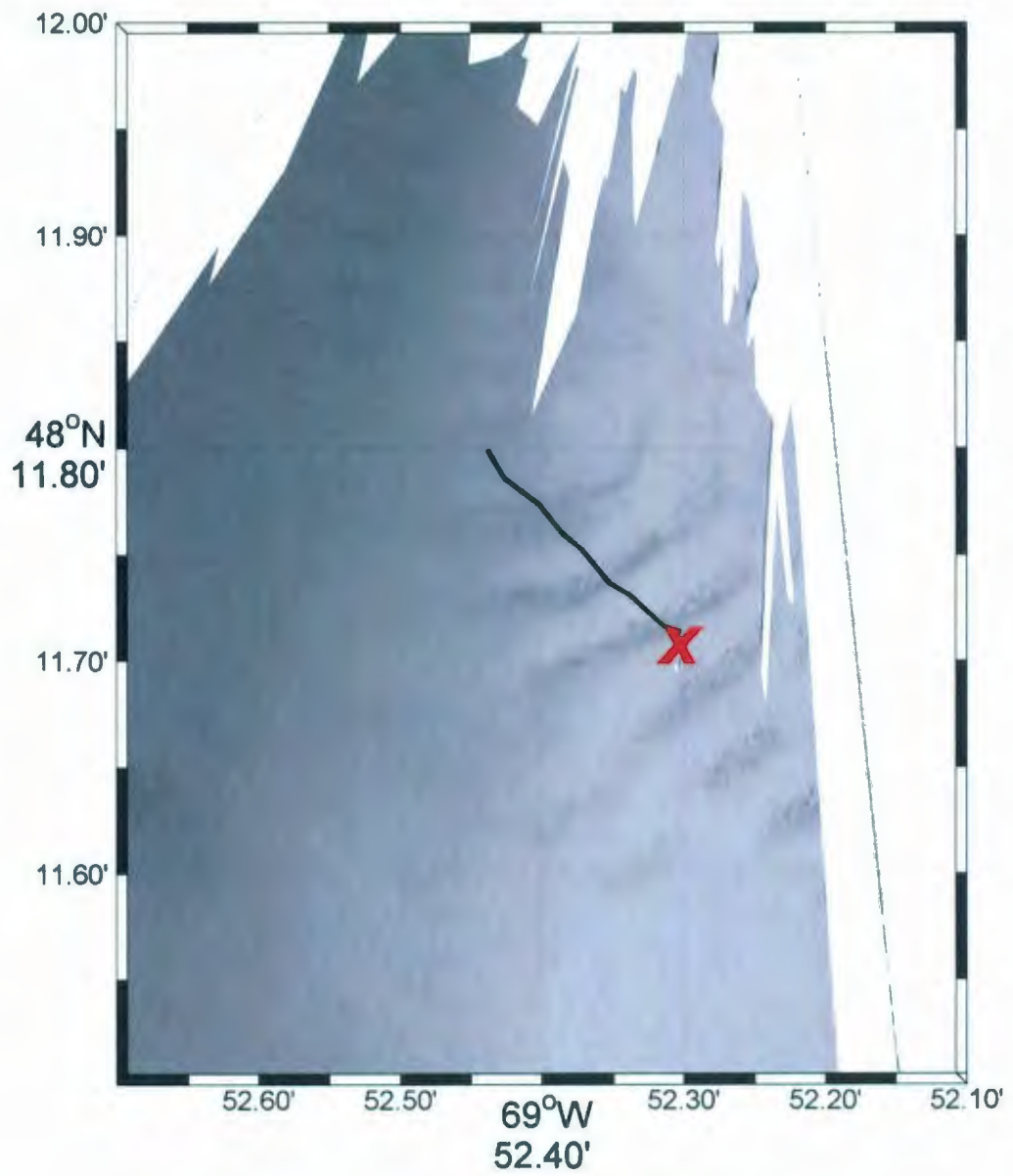


Figure 3.8: Same as Figure 3.7 for wavetrain H. The black line shows the GPS track, while the red 'X' indicates the location of the Krill.

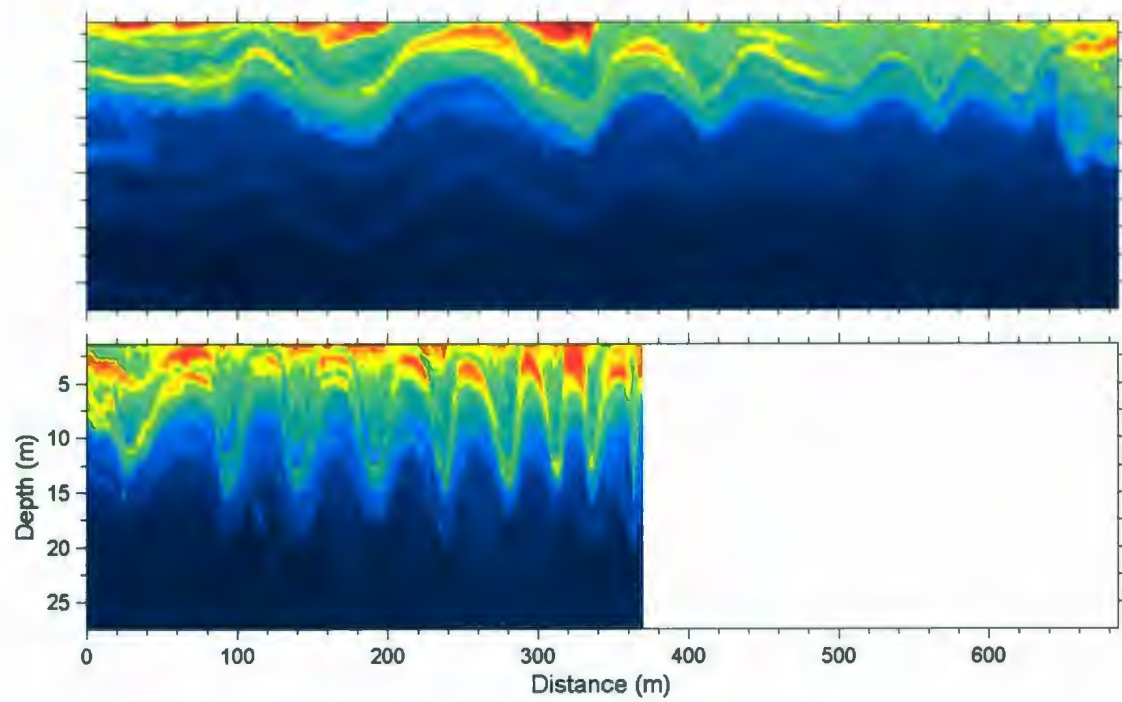


Figure 3.9: Wavetrains G and H transformed to the spatial domain.

peak to trough distance will be used instead of the amplitude as the structure of these waves can create difficulties when trying to measure a proper amplitude.

A noticeable difference seen in Figure 3.3 is from pass G to H the waves have steepened and have become more uniform. Comparing the vertical velocity plot in Figure 3.5 to that in Figure 3.6 it can be seen that the banded structure for pass H is more evenly spaced and better defined.

Using the method described in the previous section the phase speed, c , was found to have doubled from pass G to H with values of 0.08 ± 0.01 m/s and 0.16 ± 0.02 m/s, respectively.

Transforming the ADCP data for passes G and H to the spatial domain enables the wavelength to be found. Since the waves in each train are not evenly spaced, it is more informative to discuss the mean value for the wavelengths along with its range of values.

For wavetrains G and H (Figure 3.9) the mean wavelength is $L = 88(49, 136)$ m and the mean peak to trough range is $4(2, 7)$ m. The largest wavelength occurs in the leading wave and then decreases for subsequent ones after.

The average wavelength from G to H decreases by 47 m to $L = 41(28, 51)$ m while the peak to trough range increases by 5 m to $9(8, 10)$ m. Once again the waves decrease in wavelength throughout train H.

The rapid increase in amplitude and phase speed of the waves in train H lead to the question of what happens to this train. Geo-rectification images show this train continues to propagate in the same direction for approximately another 20 minutes. Unfortunately, the fate of this wavetrain was not captured with the ADCP as surface currents diverted the Krill in a different direction than that of the wave.

3.3.2 Evidence of internal wave reflection

In this section evidence of internal wave reflecting off the coastline of the fjord will be presented. It must be noted that the occurrence of internal waves reflecting were found during data analysis and there were no obvious visual indications that this phenomenon was occurring while the sampling was being performed. For this reason the Krill was not always in an optimal location to gather ADCP data about the incoming and reflecting waves. Nevertheless, we ended up collecting unusual observations showing evidence of internal wave reflection in a coastal environment. Internal wave reflection has been studied in the laboratory (e.g. Helfrich, 1992; Michallet and Ivey, 1999) and with numerical simulations (Bourgault and Kelley, 2007) but we are not aware of any field observations reporting this potentially important phenomena of internal wave propagation in coastal environments.

This section will look at two instances in which internal waves are seen approaching a shoreline and then reflected waves are observed. The first occurrence of wave reflection occurred on July 5, 2007 at Pointe aux Crêpes (Figure 3.10).

The initial wave (train E) (Figure 3.12) to hit the shoreline was sampled by the ADCP as it was part of a train that was being followed that day. The wave had an amplitude of 13 ± 1 m and was traveling at a phase speed of 0.26 ± 0.01 m/s. Figure 3.11 shows the density profile of the water column prior to the wavetrain propagating through it. Again in Figure 3.11 we see a distinct two layer density structure similar to that in Figure 3.4. The pycnocline occurs closer to the surface at approximately 2 m with a density difference of $\Delta\rho = 7 \text{ kg m}^{-3}$.

The wave crests of this train almost encompass the entire width of the fjord (Figure 3.13). Upon encountering Pointe aux Crêpes it becomes cut and one piece continues up the fjord while the other reflects off the cape. The piece which continues

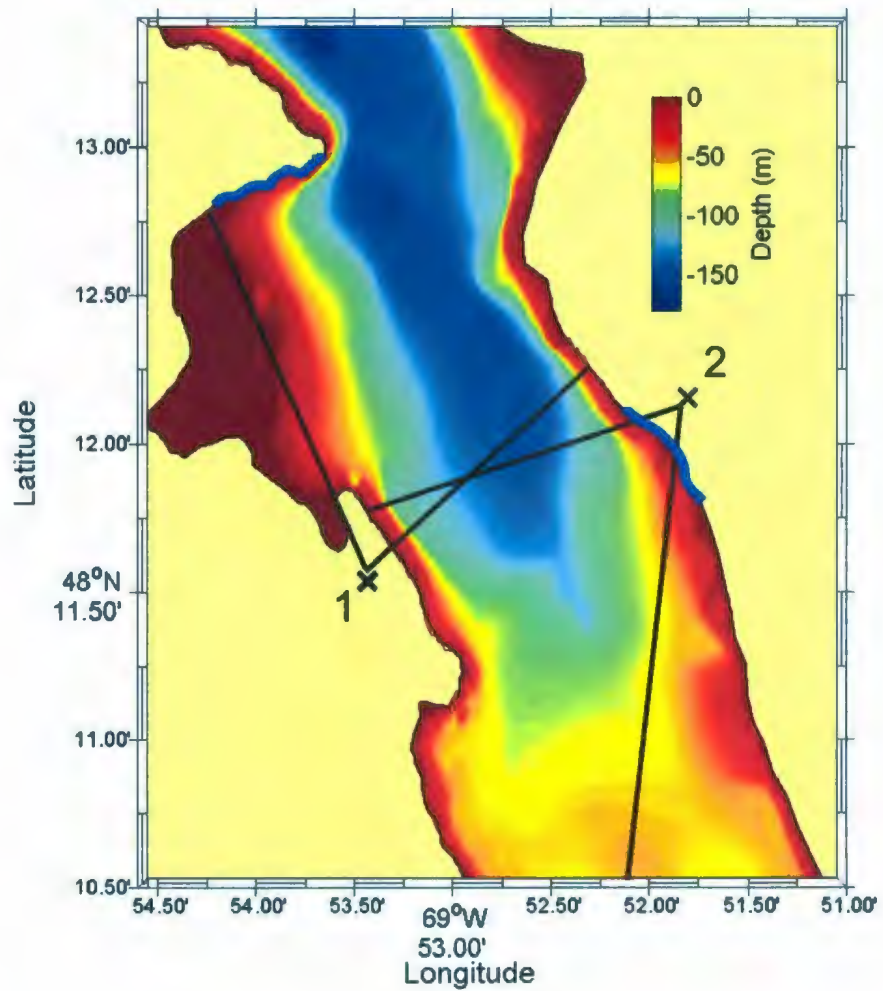


Figure 3.10: Location (X) and field of view of the camera (lines) for July 5(1) and 10(2), 2007. The blue lines on the coastline indicate where the waves reflect.

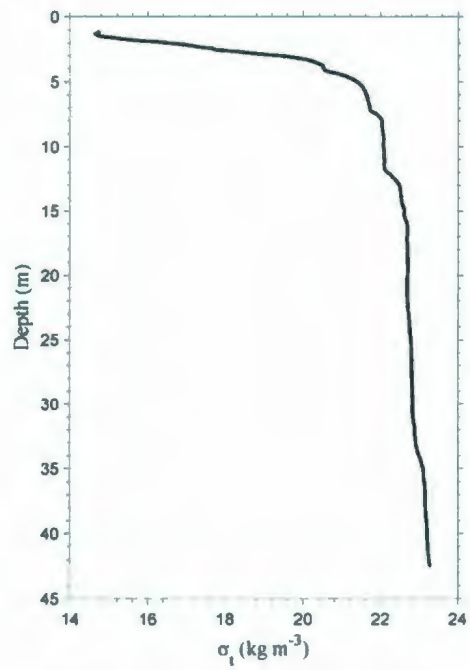


Figure 3.11: Density profile of the water column before wavetrain E propagates through.

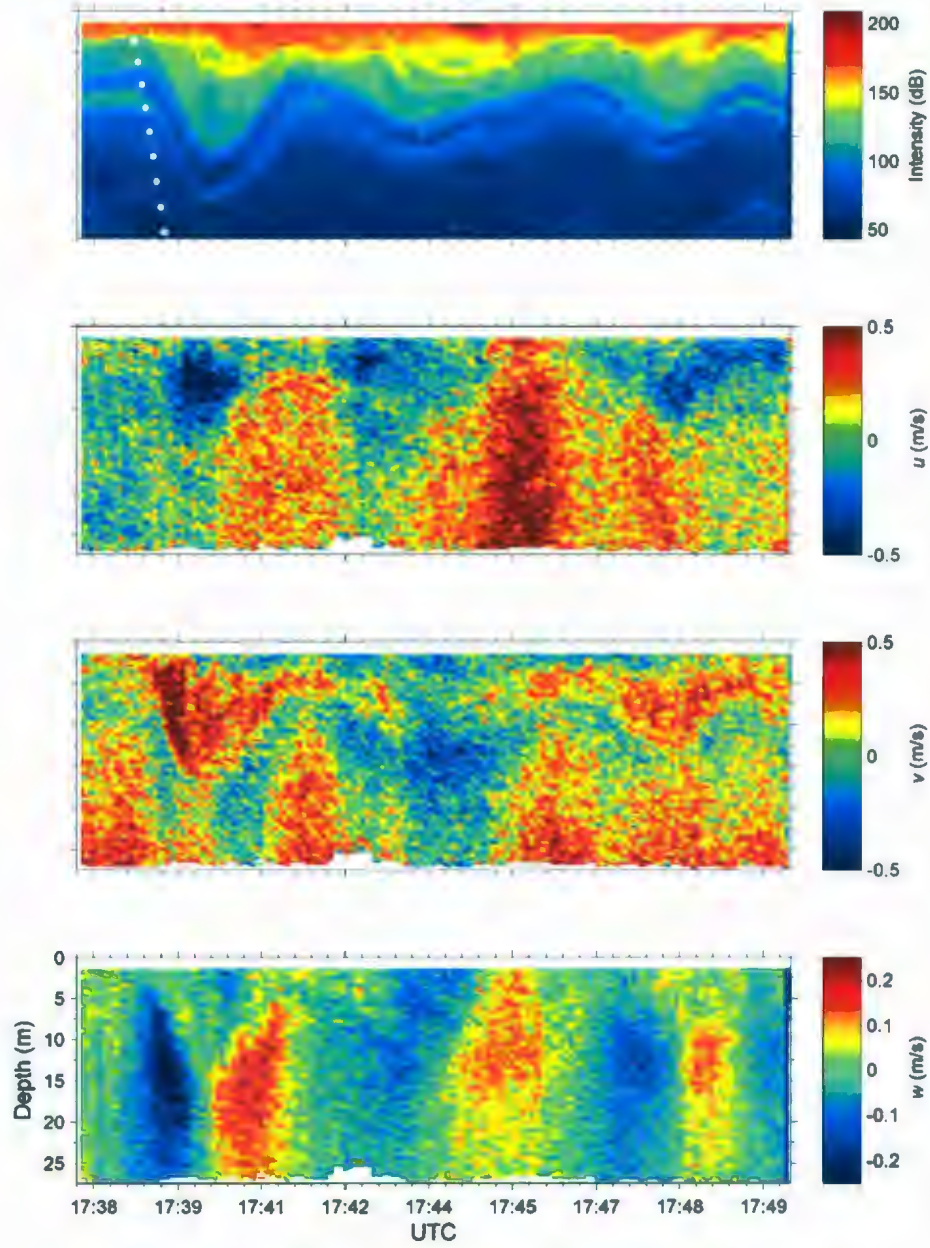


Figure 3.12: Intensity, horizontal velocities u and v , and vertical velocity w initial incoming wave on July 5, 2007 which later is reflected off the coastline.

up-channel is sampled (train F) (Figure 3.15) by the Krill approximately 10 minutes after train E. Figure 3.14 shows the GPS tracks for both E and F.

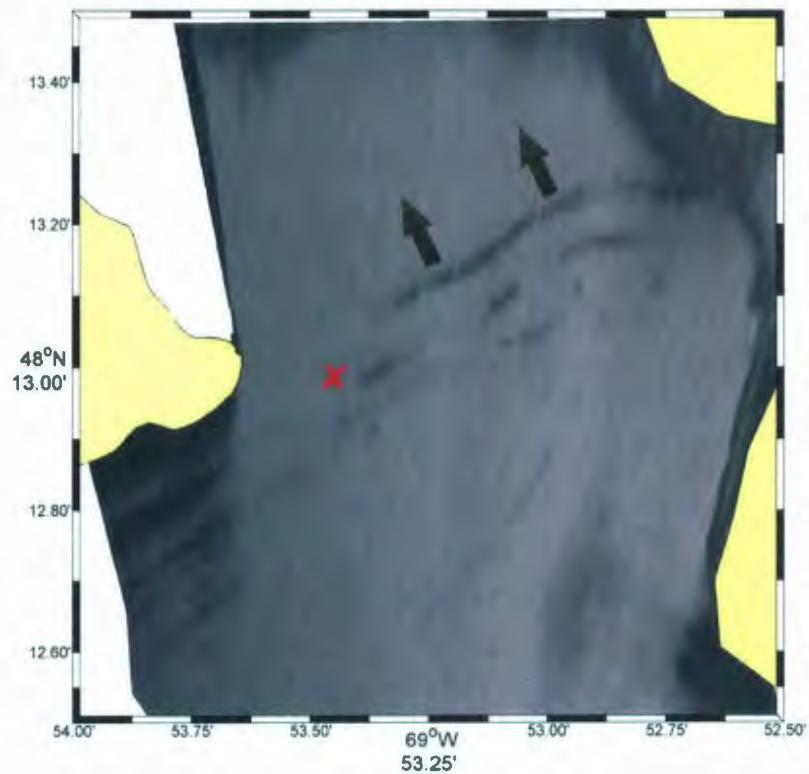


Figure 3.13: Internal wave bands spreading nearly across the entire width of the fjord prior to being 'cut' at Pointe aux Crêpes. The image was taken at 17:40 UTC. Refer to Figure 3.16 for a detailed temporal view around the cape.

Figure 3.16 shows the progression of flow from 17:40 UTC to 18:05 UTC on July 5th, 2007 using geo-rectified images. Lines have been used to highlight the surface bands caused by the internal waves with arrows indicating the direction in which the waves are propagating.

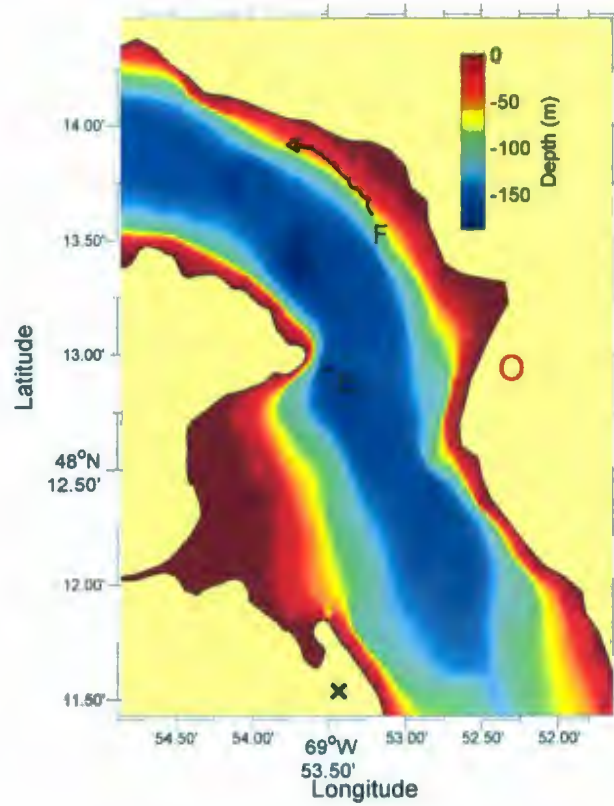


Figure 3.14: GPS tracks for train E and train F which is sampled 10 minutes later. The red circle indicates an area where a second camera would be useful to document the flow up-fjord.

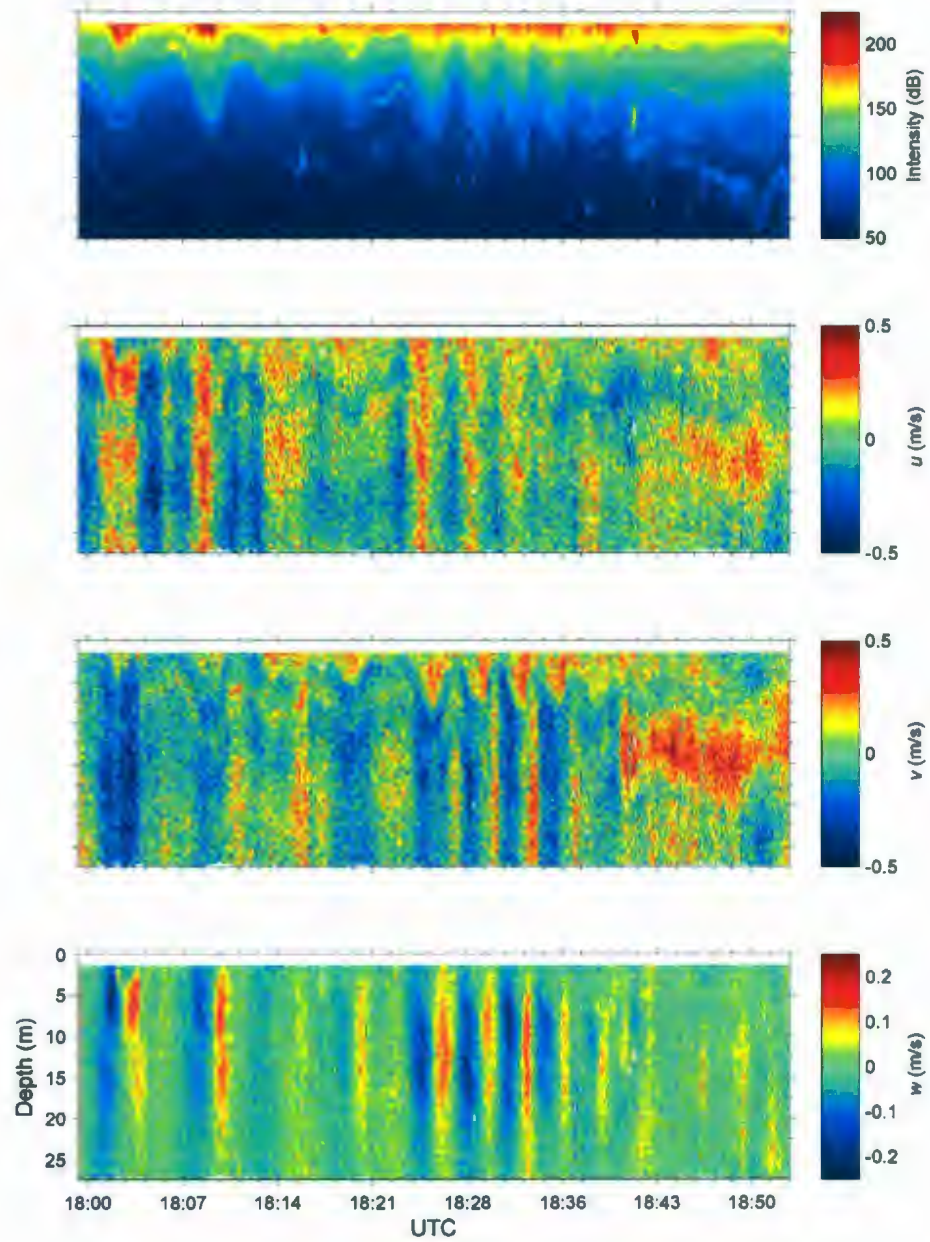


Figure 3.15: Intensity, horizontal velocities u and v , and vertical velocity w for wave-train F.

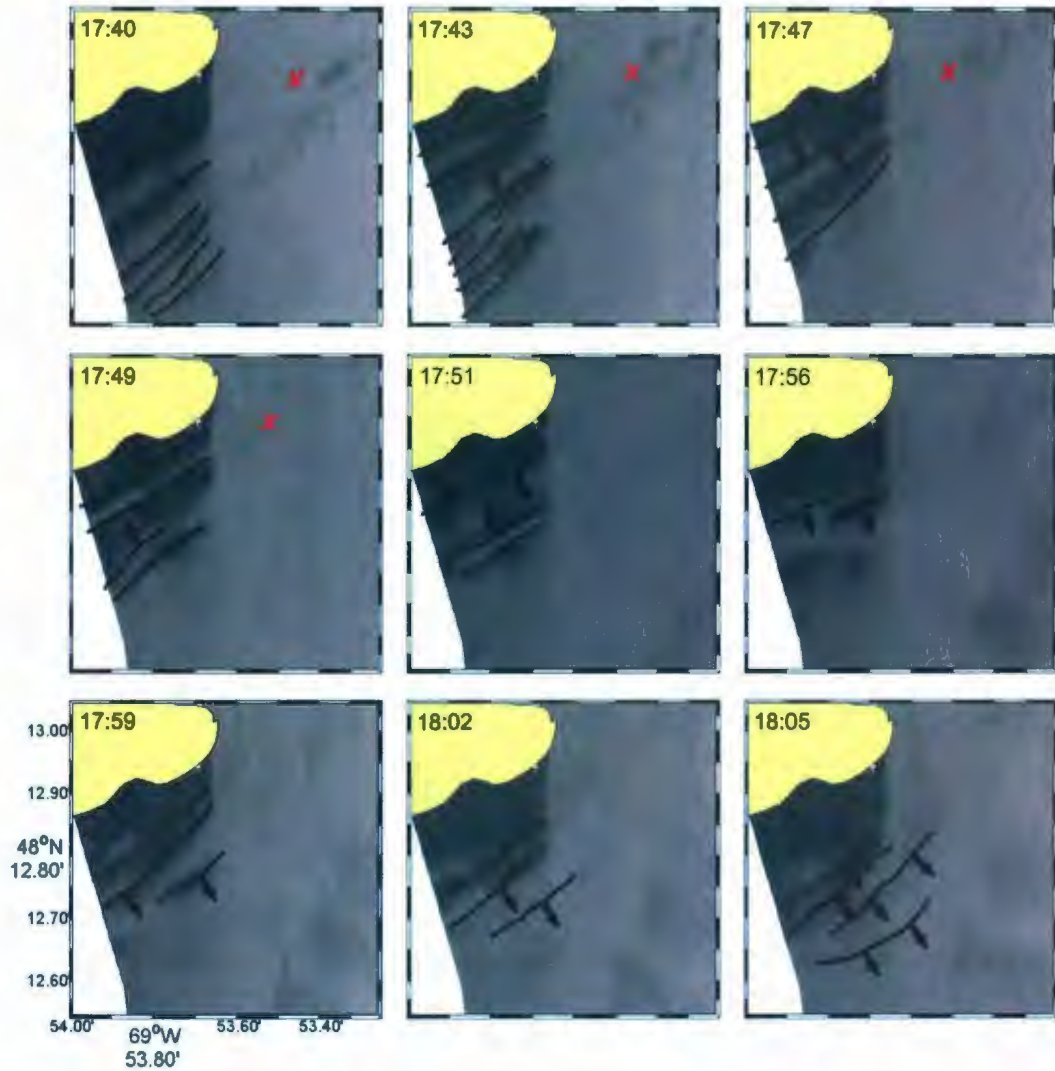


Figure 3.16: Progression figure for wave reflection on July 5, 2007. The lines correspond to the wave crests while the arrows indicate the direction the waves are propagating. The red 'X' in the first four panels indicates the location of the Krill.

From Figure 3.16 an along-channel wavetrain can be seen propagating landward and then encountering Pointe aux Crêpes. Until panel 17:51 all of the bands are propagating toward land, at which point the first reflected wave can be seen. At this point there are still waves propagating toward land. After panel 17:51 all of the bands shown correspond to reflected waves as they begin to leave the protection of the small bay they are in and move into the main body of the fjord again. Once the waves enter the main body of the fjord their surface signature disappears and the fate of these waves is unknown after this point.

The second occurrence of wave reflection was observed from the data collected July 10, 2007 in a different location (Figure 3.10) than that of July 5. The sampling boat was in the area of both the incoming and reflected waves, however, the strong mean current of the fjord forced the boat to drift down-channel toward the mouth of the fjord instead of along channel in the direction of the propagating waves. ADCP data was collected during this time but it cannot be said with certainty that either the incoming or reflected waves were sampled.

The geo-rectified images were used to find a phase speed of $0.27 \pm 0.02 \text{ m s}^{-1}$ for the incoming wavetrain. Figure 3.17 shows the progression for the wavetrain from 19:39 UTC to 20:51 UTC on July 10, again with the lines highlighting the wave crests and the arrows indicating direction of propagation. It should be noted that not all of the wave crests have been highlighted as during this period waves were found to be propagating in various directions and to highlight them all would create a crowded image.

The initial incoming waves this time are propagating cross-channel and they hit the coastline almost directly in front of the camera. The large number of surface bands during this sampling time can make it somewhat difficult to follow the incoming and reflected bands. Using animations of geo-rectified images helped in this process.

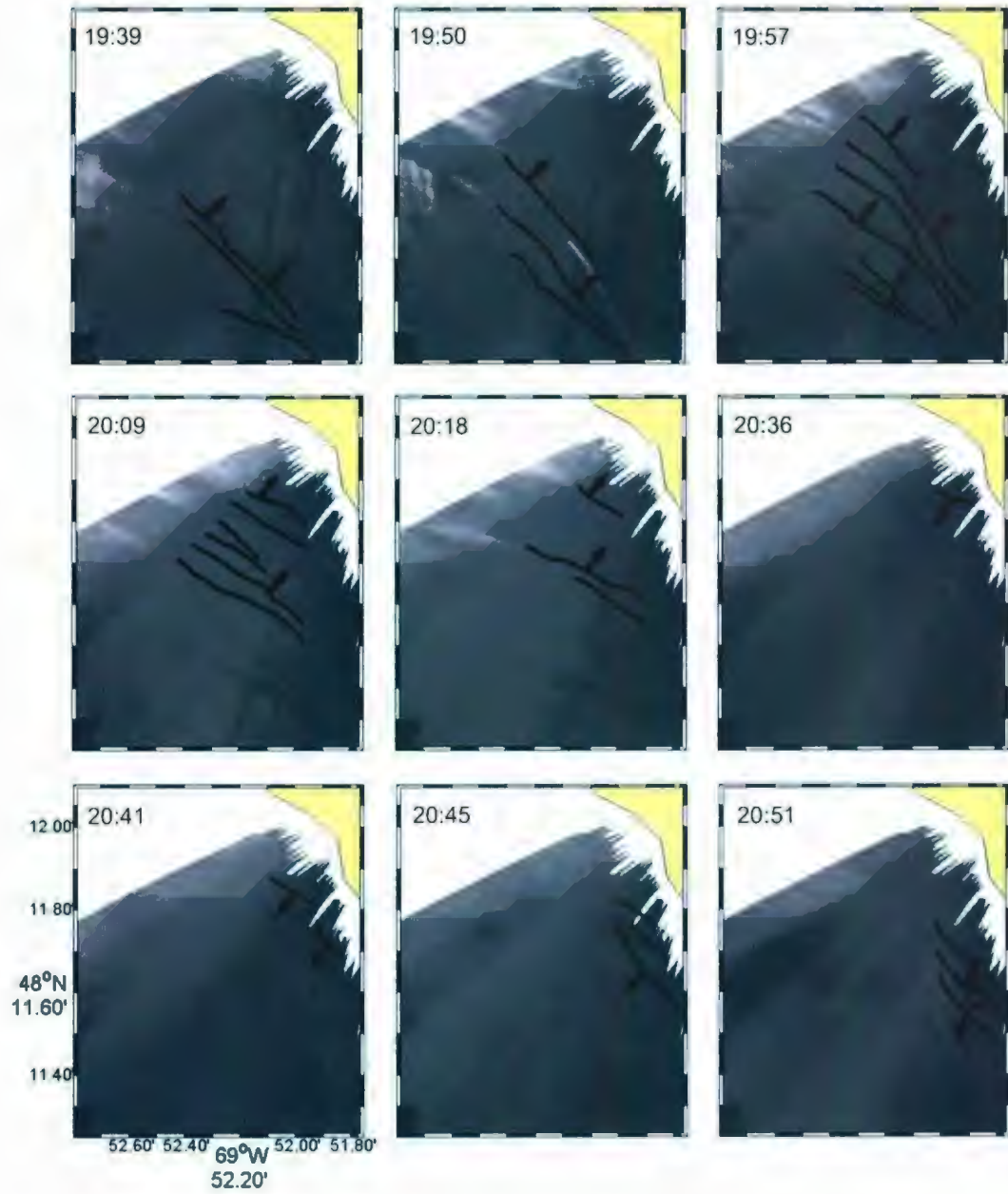


Figure 3.17: Progression figure for wave reflection on July 10, 2007.

Until panel 20:18 the waves are propagating toward land and in panel 20:36 the first reflected wave can be seen. All panels after 20:36 show the reflected waves and similar to July 5th once the waves encounter the mean current of the fjord their surface signatures disappear and their fate is unknown.

3.4 Discussion

This field study was done without any real organization outside of a rough idea of where to sample and when. Internal waves were found in various locations on the landward side of the sill, and throughout all phases of the tide, propagating in nearly every direction.

The data collected provides insight into the flow about the shallow inner sill of the Saguenay Fjord, but perhaps even more importantly it can be used to help organize a future study with more distinct goals.

For instance, having a towed body of instruments attached to the sampling boat would allow internal waves to be followed and their evolution observed (Bourgault *et al.*, 2007). This could be quite useful in determining the fate of internal wavetrains such as those presented in Section 3.3.1.

Having upward looking ADCP's moored to the sea floor near the coastline in areas which appear to promote wave reflection, like those in Figure 3.10, could also be a natural progression of study for this work. Assuming the instruments could withstand the currents in those areas they might provide valuable information toward better understanding of how internal waves interact with coastlines.

The use of still photography and geo-rectification have proven very beneficial for this field study, and the use of an additional camera would provide even more information. Having another camera positioned on the hill across the fjord (indicated

by the red 'O' in Figure 3.14), looking up-fjord would provide information as to how wavetrains similar to F evolve.

Chapter 4

Summary

The importance of the shallow inner sill of the Saguenay Fjord with respect to processes such as turbulence and internal waves was shown by the simulations discussed in Chapter 2. Areas on each side of the sill contained hot spots for kinetic energy and large-scale eddies along with internal wave trains were seen at various stages of the simulation.

Using these results in planning a field study was initially beneficial as it provided answers to where and when to sample. However, once on site the limitations caused by the two-dimensionality of the model were soon realized. Internal waves were seen propagating both along channel and cross channel which could not be simulated by the model.

The ability to sample a wavetrain more than once along with time-lapse photographs of sea surface manifestations allowed for in-depth analysis of internal waves in the Saguenay. The large-amplitude train discussed in Chapter 3 is observed to steepen as it propagates landward, along channel, away from the sill. Its wavelength is seen to decrease while its phase speed and amplitude both increase. The final fate of this train is not known as surface currents forced the Krill to drift in a different

direction than that of the wavetrain.

The internal wave reflection cases discussed in Chapter 3 are believed to be the first observations of their kind in a coastal environment. The use of shore based photography proved extremely valuable for this analysis as without them this phenomena would not have been discovered. On July 5th the internal wave which encounters Pointe aux Crêpes is nearly the entire width of the fjord as it propagates along channel. This wave is observed to cut in half at the cape with one piece reflecting and the other continuing up-fjord. The other case of internal wave reflection occurs when a cross channel internal wave hits the shoreline and reflects back. In both cases sampling from the Krill did not capture the incoming and reflecting waves as there was no evidence while on site that wave reflection was occurring.

The simulations and field work presented in this thesis provides insight into the area of the shallow inner sill of the Saguenay Fjord. They can now act as a guideline for further research with more exact objectives, for example in the area of internal wave reflection and propagation.

Bibliography

- [*Afanasyev and Peltier(2001)*] Afanasyev, Y. D., and W. R. Peltier (2001), On the breaking internal waves over the sill in Knight Inlet, *Proc. R. Soc. Lond. A*, *457*, 2799–2825.
- [*Baines(1984)*] Baines, P. G. (1984), A unified description of two-layer flow over topography, *J. Fluid Mech.*, *146*, 127–167.
- [*Baker and Pond(1995)*] Baker, P., and S. Pond (1995), The low-frequency residual circulation in knight inlet, british columbia, *J. Phys. Oceanogr.*, *25*, 747–763.
- [*Bélanger(2003)*] Bélanger, C. (2003), Observation and modelling of a renewal event in the Saguenay Fjord, Ph.D. thesis, Université du Québec à Rimouski, Rimouski, Québec.
- [*Bourgault(2008)*] Bourgault, D. (2008), Shore-based photogrammetry of river ice, *Can. J. Civ. Eng.*, *35*, 80–86.
- [*Bourgault and Kelley(2003)*] Bourgault, D., and D. E. Kelley (2003), Wave-induced boundary mixing in a partially mixed estuary, *J. Mar. Res.*, *61*(5), 553–576.
- [*Bourgault and Kelley(2004)*] Bourgault, D., and D. E. Kelley (2004), A laterally averaged nonhydrostatic ocean model, *J. Atmos. Oceanic Technol.*, *21*(12), 1910–1924.

- [*Bourgault and Kelley(2007)*] Bourgault, D., and D. E. Kelley (2007), On the reflectance of uniform slopes for normally incident interfacial solitary waves, *J. Phys. Oceanogr.*, *In press*.
- [*Bourgault et al.(2007)**Bourgault, Blokhina, Mirshak, and Kelley*] Bourgault, D., M. Blokhina, R. Mirshak, and D. E. Kelley (2007), Evolution of a shoaling internal solitary wavetrain, *Geophys. Res. Lett.*, *34*, L03,601, doi:10.1029/2006GL028,462.
- [*Cummins et al.(2003)**Cummins, Vagle, Armi, and Farmer*] Cummins, P. F., S. Vagle, L. Armi, and D. M. Farmer (2003), Stratified flow over topography: upstream influence and generation of nonlinear internal waves, *Proc. R. Soc. Lond. A*, *459*, 1467–1487.
- [*Farmer and Armi(1999)*] Farmer, D. M., and L. Armi (1999), The generation and trapping of internal solitary waves over topography, *Science*, *283*(5398), 188–190.
- [*Farmer and Freeland(1983)*] Farmer, D. M., and H. Freeland (1983), The physical oceanography of fjords, *Progr. Oceanogr.*, *12*(2), 147–220.
- [*Helfrich(1992)*] Helfrich, K. R. (1992), Internal solitary wave breaking and run-up on a uniform slope, *J. Fluid Mech.*, *243*, 133–154.
- [*Klymak and Gregg(2001)*] Klymak, J. M., and M. C. Gregg (2001), The three-dimensional nature of flow near a sill, *J. Geophys. Res.*, *106*, 22,295–22,311.
- [*Klymak and Gregg(2003)*] Klymak, J. M., and M. C. Gregg (2003), Tidally generated turbulence over the Knight Inlet sill, *J. Phys. Oceanogr.*, submitted to *J. Phys. Oceanogr.*

- [*Lamb(2004)*] Lamb, K. G. (2004), On boundary-layer separation and internal wave generation at the Knight Inlet sill, *Proc. R. Soc. Lond. A*, *460*, 2305–2337.
- [*Michallet and Ivey(1999)*] Michallet, H., and G. N. Ivey (1999), Experiments on mixing due to internal solitary waves breaking on uniform slopes, *J. Geophys. Res.*, *104*(C6), 13,467–13,477.
- [*Osborn(1974)*] Osborn, T. R. (1974), Vertical profiling of velocity microstructure, *J. Phys. Oceanogr.*, *4*, 109–115.
- [*Pawlowicz(2003)*] Pawlowicz, R. (2003), Quantitative visualization of geophysical flows using digital oblique time-lapse imaging, *IEEE J. Oceanic. Eng.*, *28*(4), 699–710.
- [*Smagorinsky(1963)*] Smagorinsky, J. (1963), General circulation experiments with primitive equations. I. The basic experiment, *Monthly Weather Rev.*, *91*(3), 99–164.
- [*Stacey and Gratton(2001)*] Stacey, M. W., and Y. Gratton (2001), The energetics, and tidally induced reverse renewal in a two-silled fjord, *J. Phys. Oceanogr.*, in press.
- [*Trujillo and Thurman(2005)*] Trujillo, A. P., and H. V. Thurman (2005), *Essentials of Oceanography, Eighth Edition*, 532 pp., Pearson Prentice Hall, Upper Saddle River.

Appendix A

Geo-rectification how-to

A.1 Introduction

With the advent of high resolution, relatively cheap digital cameras with large power and storage capabilities georectification can provide a very cost effective method for obtaining quantitative information of coastal sea oceanographic processes. This appendix explains how to perform georectification of highly oblique images using the method described in Bourgault(2008).

A.2 On-Site Set-Up

Prior to taking the first picture it is important to ensure that any electronic equipment is set to the exact same time (i.e. camera, GPS, watch, etc). We have found it useful to set everything to UTC, to stay consistent. This makes it much easier to organize data later on, especially if you are going to compare to other information such as ADCP tracks or VMP profiles.

Equipment needed on-site for taking pictures:

- digital camera with capability to snap a photo at desired intervals
- tripod
- sufficient battery and memory reserves
- GPS

A suitable site would be at the highest possible elevation which gives you a clear view of the desired area. It is also important to find an area which has in its view some points of known latitude and longitude. These points will be referred in this document as ground control points (GCPs). The georectification scripts will require these GCPs as reference.

Once the camera is set up it is important that it not be moved throughout the process. This can be somewhat difficult when it comes to switching batteries and memory cards. If it is necessary to tilt the camera either in the vertical or horizontal make sure that you document the estimated degree to which you do so. This will aid the algorithms later when they try to minimize the error in the georectification.

Once you take the first picture it is a good idea to document time as well as the latitude, longitude, elevation and error associated with the GPS.

A.3 Rectification

A.3.1 g_rect package

To perform the georectification the user will require the g_rect package which contains eight .m files:

- g_dist.m

- `g_error_geofit.m`
- `g_error_polyfit.m`
- `g_pix2xy.m`
- `g_poly.m`
- `g_rect.m`
- `g_viz.m`
- `g_xy2ll.m`

None of these `.m` files require any changes by the user; rather the set of photos has a `.dat` file associated with it which contains all pertinent information.

`g_viz.m` also requires the use of the Matlab package `m_map`, which can be downloaded from Rich Pawlowicz's Matlab Stuff website (<http://www2.ocgy.ubc.ca/rich/index.html>).

A.4 `.dat` file

The first section of the `.dat` file asks for input/output information; `img_fname` is the name of the image to be used for the georectification, `first_img_fname` and `last_img_fname` are the first and last images of the set respectively, and `out_fname` is the name of the output `.mat` file created.

The camera position should be recorded as accurately as possible with West and South being negative. `fov` is the field of view of the camera and can generally be obtained from the owner's manual or calculated. The remaining parameters have sufficient explanation in the file, but require a "best guess" in some instances. The camera altitude should be given in meters. The associated uncertainties also require the user to estimate their value.

jsky is a variable which allows the user to limit the amount of the image which is shown. This can be useful when an image contains a lot of sky and the interest is on the water, thus '*jsky*' number of pixels will be removed from the top of the image, resulting in a faster display.

In order to accelerate the minimization there is an option to skip pixels. While this is not recommended for the final product it can be quite useful when trying to determine initial guess for the poorly known parameters. Skipping every 5 or 10 pixels will give you a quick set of parameters which can then be used as initial guesses.

To complete the .dat file the GCPs must be established.

A.5 Ground Control Points

The GCPs can come from different sources, preferably a fixed location such as a buoy or land mass, or if a boat fitted with GPS is in the image it can also be used. Examples of each follow.

Figure A.1 was taken in the Saguenay Fjord on July 9th, 2007. It is important to try and obtain GCPs that will cover as much of the field of view as possible. It is absolutely necessary to have at least as many GCPs as parameters which need to be minimized. That is, parameters which are not 100% known (i.e. tilt angle, camera height, view angle, dip angle, and potentially the horizontal field of view). Refer to Bourgault (2008) for a clearer description of these parameters. Generally, it is a good idea to obtain at least six GCPs.

Figure A.2 is a zoom of the boat so a x and y pixel can be chosen. In practice it may be beneficial to zoom in more. There is obviously some error associated with this process, and as a result choosing the pixels can be difficult.

In this case it is known that the GPS was located toward the bow of the boat



Figure A.1: Sample image of the Saguenay Fjord. (a) highlights a boat which has a GPS and the corresponding lat and lon can be obtained for the time this picture was taken. (b) highlights a small cape whose lat and lon can easily be obtained from a marine chart.



Figure A.2: Zoom of the boat in order to obtain the x and y pixels.

so a choice of 1651 for the x-pixel is reasonable. As for the y-pixel it is important to choose a pixel which corresponds to the point at which the boat is in the water, not a point at the top of the boat. This is due to the fact that a 2-D image cannot account for elevation and as a result a pixel chosen at top of the boat would actually correspond to an area in the background. In this case 1360 was chosen as the y-pixel. Knowing the exact time when this image was taken allows us to check the GPS data from the boat and then we have a GCP. This is then repeated with the boat in as many images as are needed to encompass maximum area.

Case (b) is shown in Figure A.3. Once again in practice the image would be zoomed in much more.



Figure A.3: Zoom of the cape in order to obtain x and y pixels.

Again it is important to chose pixels at the point which the land comes in contact with the water and not on the land itself. For this particular point a x-pixel of 793

and a y-pixel of 885 was chosen. Then using a marine chart the corresponding lat and lon were found.

The GCPs need to be organized in tabular form (Table A.1), and added to the .dat file.

A.6 g_rect.m

Ensure that the path has been set to the g_rect package. The georectification can be ran from the Matlab command window by simply typing *g_rect*. A prompt will ask for the name of the .dat file and once entered the georectification will begin.

The command window will display all the input parameters and a figure window will show the image being rectified, along with all the GCPs. It is important at this step to make sure all the GCPs are where they should be as it is easy to make a mistake. If you are satisfied with the locations of the GCPs type 'y' to proceed with the rectification.

A.7 show_rectification.m

The script show_rectification.m is set up as a function which can simply be ran in the Command Window or called by another script.

Depending on the naming convention used for the images the user will have to adjust the section *Image name* to meet their needs. *Map Range* allows the user to set the limits for longitude and latitude which will be displayed. The user can then load coastline data if they have any, if not the final section of this script (*Filling the land*) should be commented out.

There is also the option to plot the ground control points along with the image

Table A.1: gcp.dat created for July 9th, 2007 images. West and South are considered to be negative (-).

x-pixel	y-pixel	LON	LAT
1650	1244	-69.8749137	48.1966138
1420	1223	-69.8735404	48.1964636
1164	1209	-69.8729181	48.196013
970	1196	-69.8724246	48.1956482
768	1190	-69.8719096	48.1953692
580	1186	-69.8713303	48.1950903
429	1182	-69.8707509	48.1948543
204	1179	-69.8698926	48.194468
2037	1371	-69.8741198	48.1989527
1651	1360	-69.8734546	48.1986737
1296	1363	-69.8727679	48.1985235
861	1370	-69.8718882	48.1984162
334	1378	-69.8705578	48.198266
1646	1459	-69.8729396	48.1994891
1356	1591	-69.8719311	48.2004333
376	1358	-69.8704076	48.19803
667	876	-69.87375	48.16091667
793	882	-69.87466667	48.16625
1325	885	-69.88008333	48.16975
1685	900	-69.88266667	48.1745
2428	963	-69.88291667	48.18616667
2550	986	-69.88275	48.18766667

control point. This can be done by uncommenting the section *Plot GCPs and ICPs*. It is a good idea to do this at least once to see how well the control points for the image match up with the actual ground control points.

Figure A.4 shows the full rectified image for one of the photos.

While Figure A.4 is useful it can sometimes be more informative to zoom over certain areas, especially if looking for things such as internal waves. Figure A.5 shows a nice internal wavetrain.

As this how-to is just a basic template on how to use the georectification scripts it does not go into detail with some of the options. The user can adjust the scripts to fit his or her needs.

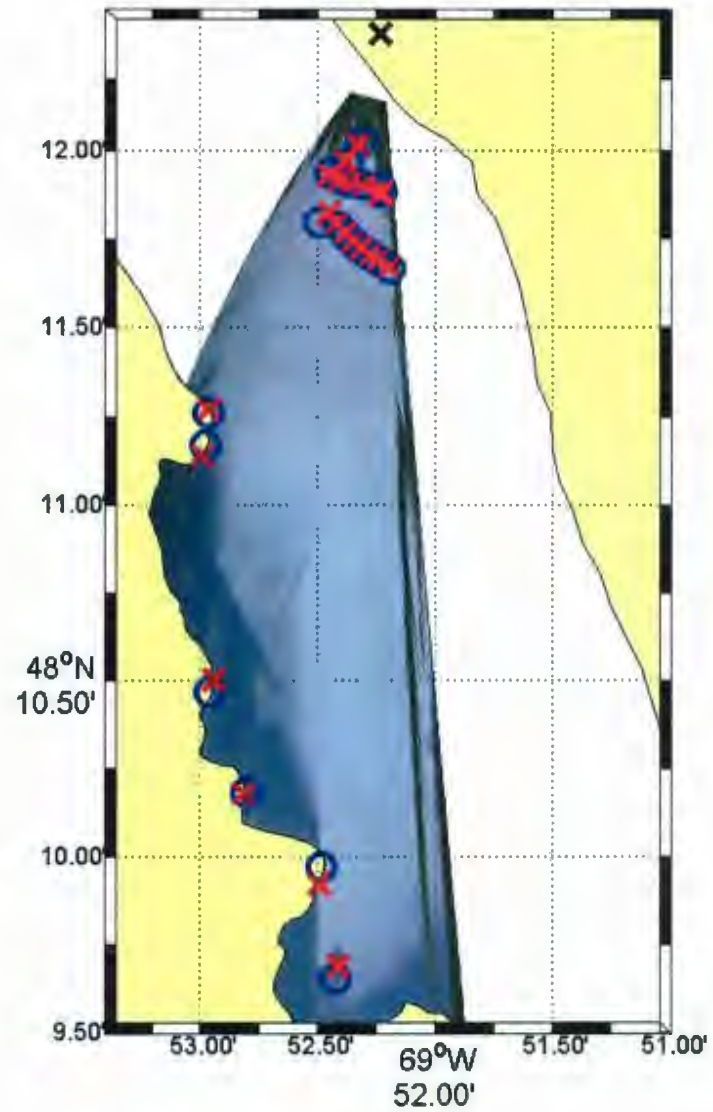


Figure A.4: Full rectified image. GCPs are show as red x's and ICPs are blue circles. The black x indicates the location of the camera.

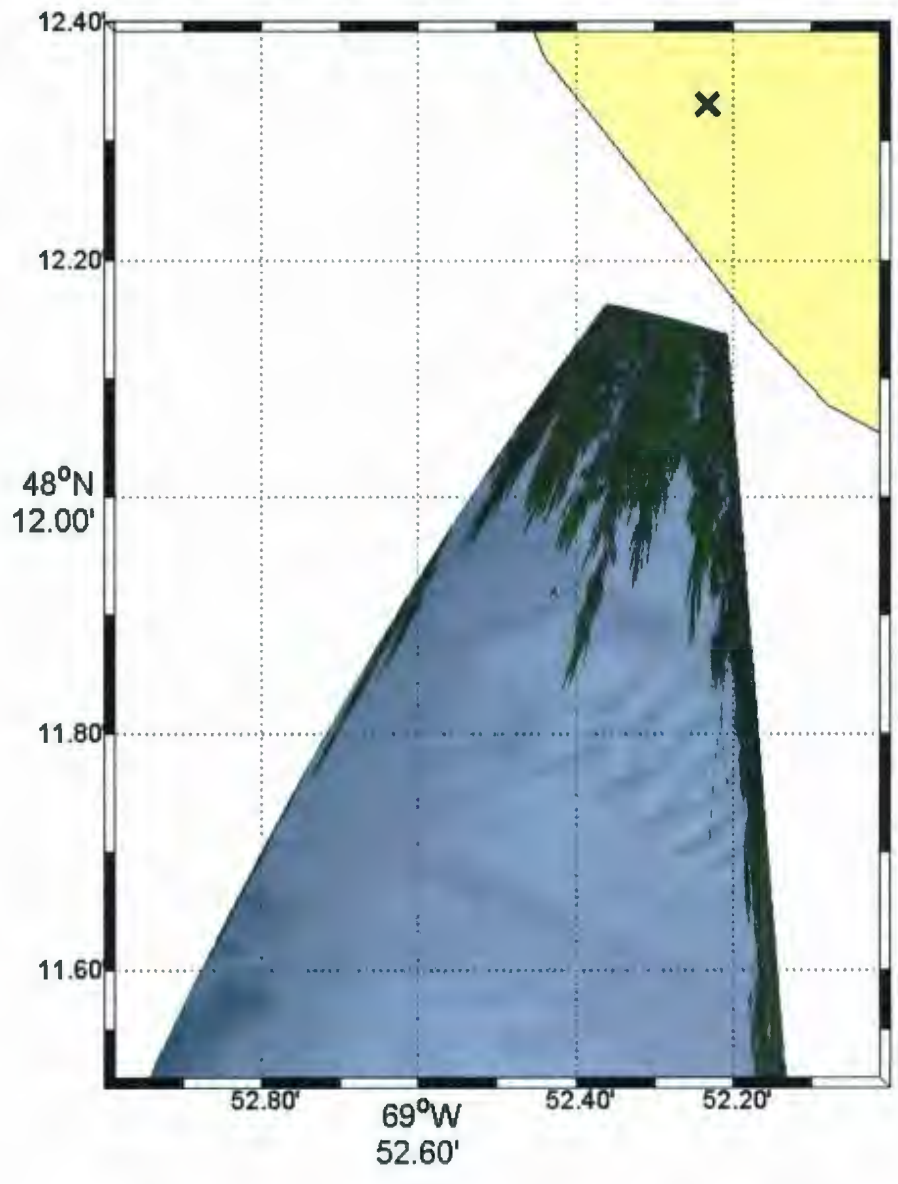


Figure A.5: Zoom of rectified image showing internal wavetrain.

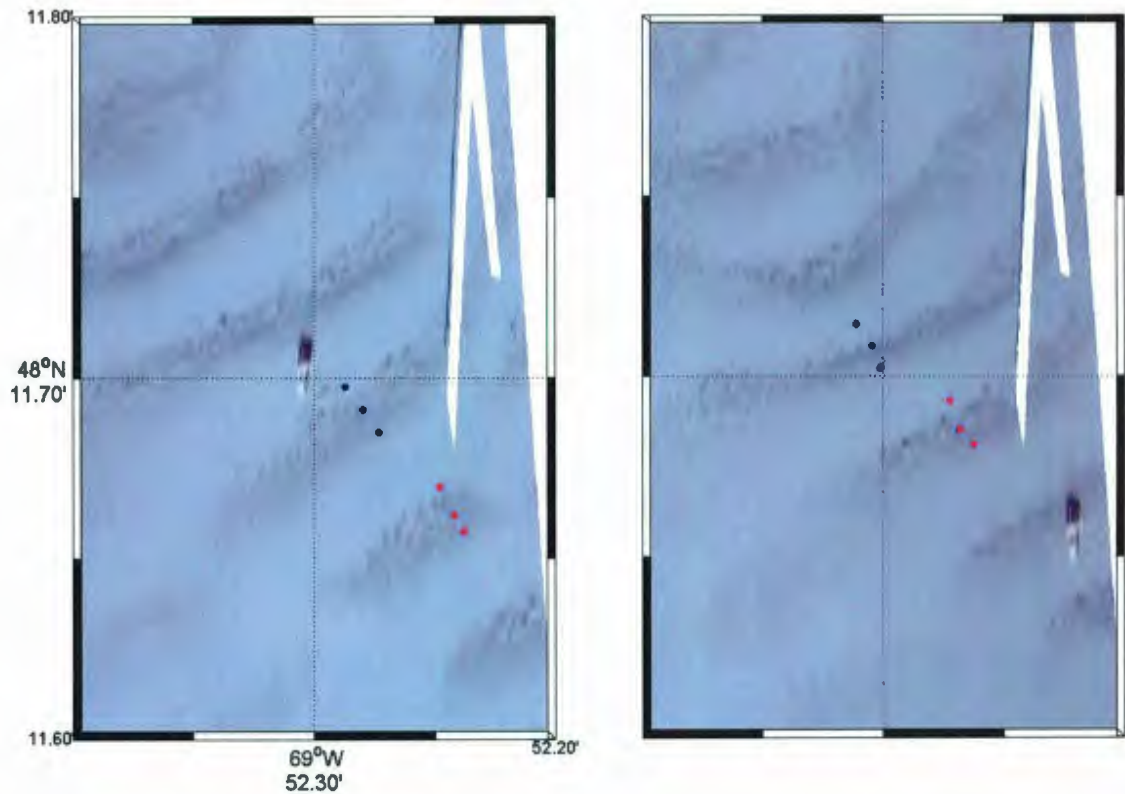


Figure B.1: Two georectified images spaced five minutes apart are used to calculate the phase speed of the internal wavetrain. The latitude and longitude of the black (red) dots on the left panel along with those from the right panel are used to find the distance traveled by the wavetrain in five minutes.

points is used to calculate the wavelength for that wave. The average value for the wavelength from this method is 54 ± 1 m.

By comparison, Figure B.3 shows the remapped ADCP intensity plot along with six crosses. Again, each pair of crosses is used to find the wavelength of the same internal wave as that in the rectified image. The average wavelength from this method is 51 ± 3 m.

Since these wavelengths agree within uncertainty this method will be used for the purpose of this thesis.

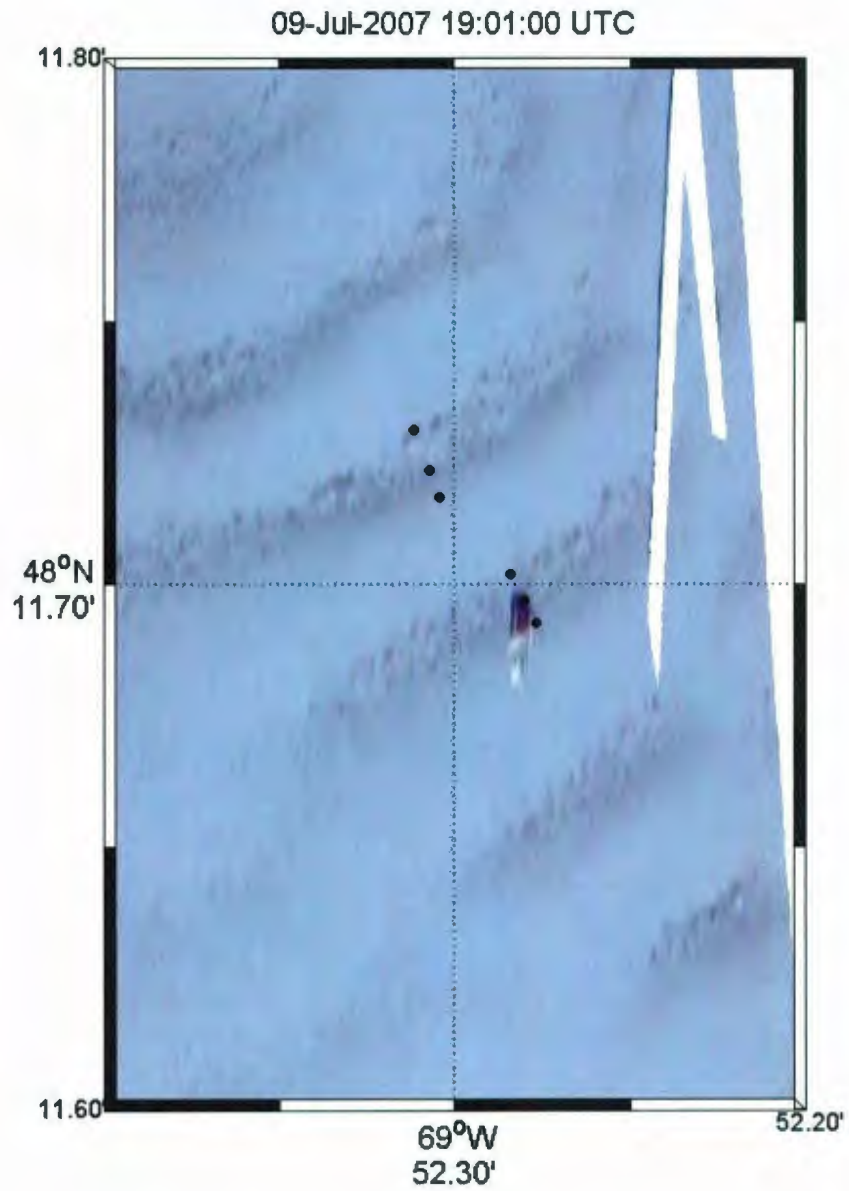


Figure B.2: Three dots on one wave crest are matched with the corresponding ones on another crest to find the wavelength of the internal wavetrain. The result is the average of the values.

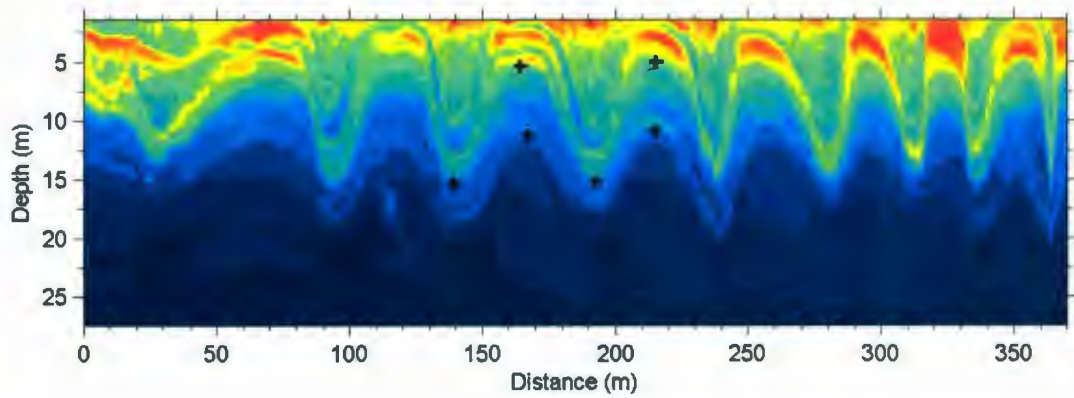


Figure B.3: In two cases the peak to peak distance is used to find the wavelength, while in another the trough to trough distance is used. The average value is used to compare to that obtained from Figure B.2





